Ionospheric Signatures of Solar Flares

by

Etienne Koen

Submitted in fulfilment of the requirements for the degree of Master of Science in the School of Physics, University of KwaZulu-Natal.

As the candidate's Supervisor I have/have not approved this thesis/dissertation for submission

Signed: ..... Name: ..... Date: .....

Durban, 2009.

Abstract

VLF waves propagate in the Earth-ionosphere waveguide (EIW). The EIW is bounded below by the surface of the Earth and above by the ionospheric D-region (50–90 km altitude). The conditions for wave propagation in the EIW are studied and derived specifically for VLF propagation. The D-region is maintained by shortwave solar radiation that ionises the neutral atmosphere. The Wait parameters, H' (reflection height) and β (sharpness), describe the lower boundary of the D-region. Any enhancement in solar X-rays modifies these parameters, leading to a change in the propagation conditions for VLF signals. The effect of the terminator is presented where, it is found to narrow the depression of the monthly averaged diurnal amplitude profile from summer to winter. A series of solar flares were identified of which two case studies are presented. H' and β are calculated from the VLF signals by the Long Wave Propagation Code (LWPC). It is found that H' decreased and β increased at the time of flare. Once H' and β are obtained, the electron density profile can be constructed which is of crucial importance for VLF waves propagating in the EIW. The gradient of the electron density profile is found to increase as β increases. It's found that all the modal interference minima are moved towards the transmitter at the time of the flare. For flares of great magnitude, extrapolation is required to classify the flare in a magnitude class using VLF data. The change in the phase of the VLF signal is found to be linearly proportional to the change in the X-ray flux.

PREFACE

The experimental work described in this dissertation was carried out at the Hermanus Magnetic Observatory, Hermanus, and in the School of Physics, University of KwaZulu-Natal, Durban, from July 2008 to June 2009 under the supervision of Dr Andrew B. Collier.

These studies represent original work by the author and have not otherwise been submitted in any form for any degree or diploma to any tertiary institution. Where use has been made of the work of others it is duly acknowledged in the text.

DECLARATION 1 - PLAGIARISM

I, ..., declare that

1. The research reported in this thesis, except where otherwise indicated, is my original research.
2. This thesis has not been submitted for any degree or examination at any other university.
3. This thesis does not contain other persons' data, pictures, graphs or other information, unless specifically acknowledged as being sourced from other persons.
4. This thesis does not contain other persons' writing, unless specifically acknowledged as being sourced from other researchers. Where other written sources have been quoted, then:
   (a) Their words have been re-written but the general information attributed to them has been referenced
   (b) Where their exact words have been used, then their writing has been placed in italics and inside quotation marks, and referenced.
5. This thesis does not contain text, graphics or tables copied and pasted from the Internet, unless specifically acknowledged, and the source being detailed in the thesis and in the References sections.

Signed: .....

DECLARATION 2 - PUBLICATIONS

DETAILS OF CONTRIBUTION TO PUBLICATIONS that form part and/or include research presented in this thesis (include publications in preparation, submitted, *in press* and published and give details of the contributions of each author to the experimental work and writing of each publication)

No publications resulted from this research.

Signed: .....

Dedication

"Therefore, whether you eat or drink, or whatever you do,
do all to the glory of God."

- 1 Corinthians 10:31

To the Creator, my Lord and Saviour, Jesus Christ.

Acknowledgements

I would like to thank the National Astrophysics and Space Science Programme (NASSP) for funding me for the duration of my degree. Thank you to the Hermanus Magnetic Observatory (HMO) for the pleasant stay and support you have given me. I would like to thank my supervisor Dr Andrew Collier for his support, guidance and input given throughout this thesis. Thank you to Neil Thomson for always responding to my emails with great enthusiasm and for being a great help. Thank you Mom and Dad for your parental support, love and always showing an interest in my study career. Thank you to all my brothers and sisters in Christ Jesus, especially Nico Smit for giving a hand in tough times. Most of all I want to thank my Creator, Lord and Saviour, Jesus Christ by whom I'm being saved, transformed into His image and inspired by His Holy Spirit!

Contents

List of Figures

List of Tables

Acronyms

CME Coronal Mass Ejection

EIW Earth-ionosphere waveguide

GCP Great Circle Path

GIC Geomagnetically Induced Current

LWPC Long Wave Propagation Code

LWPM Long Wave Propagation Model

NOSC Naval Ocean Systems Center

SPIDR Space Physics Interactive Data Resource

TE transverse electric

TEM transverse electromagnetic

TM transverse magnetic

SPA Sudden Phase Anomaly

VLF Very Low Frequency

Chapter 1

Introduction

Solar flares are violent explosions in the Sun's chromosphere which release a huge number of energetic particles, accompanied by a rapid and intense increase in brightness. Typically the power that is released during a solar flare is in the order of 10^{20} W. Large flares can have energies up to 10^{25} J which is ten million times greater than the energy released from a volcanic eruption. Radiation is also produced from these solar flares that covers the entire electromagnetic spectrum from radio waves to gamma rays. Solar flares are generally observed above the Earth's atmosphere by dedicated satellites such as GOES, which continually measure X-ray flux in two wavelength bands: short (0.05-0.4 nm) and long, (0.1–0.8 nm). X-ray solar flares are usually classified by a magnitude index:

- B being less than 1 $\mu W/m^2$
- C being 1–9 $\mu W/m^2$,
- M being 10–90 $\mu W/m^2$ and
- X being associated with greater than 0.1 mW/m^2.

The magnitude for a specific class flare (C, M or X) increases linearly with the numeric index, e.g. C1–C9.

The magnetic energy that is built up in the Sun's atmosphere and released into the solar atmosphere comes in the form of particles such as electrons, protons and heavy nuclei and is sometimes referred to as Coronal Mass Ejections (CMEs). In most cases CMEs are also accompanied by solar flares but there is not necessarily a causal link. The monitoring of solar-flux in the event of a solar flare can act as a warning system for impending geomagnetic storms. Some threats of solar flares are to produce Geomagnetically Induced Currents (GICs) that cause the disruption of main power supplies. They can also be very harmful to astronauts and spacecraft and interfere with radio communications.

The greatest effects of solar flares on the ionosphere are seen in the D-region, 50–90 km above the Earth's surface. The day side of this region of the ionosphere is mainly maintained by solar Lyman-α radiation which ionises the minor neutral constitute nitric oxide. Although rocket experiments are mostly responsible for extracting important parameters in this region, VLF observations are used to monitor the ionosphere on a continuous basis. VLF waves propagate in the Earth-ionosphere waveguide (EIW) for paths over a few Mm with low attenuation. The Earth's surface and the base of the ionosphere are good conductors at VLF and serve as the lower and upper boundaries of the EIW. The Earth's surface is considered to be a good conductor, especially over sea regions but is not good over snow. The reflection height of the ionosphere varies with the time of the day and location.

1.1 Outline

This thesis will firstly study the quiet conditions for VLF observations, specifically the terminator effect and the depression of the monthly averaged diurnal amplitude profile. An attempt will be made to calculate the ionospheric parameters during an ionospheric disturbance caused by a solar flare. Previously the reflection height has been found to decrease and the sharpness parameter to increase during a solar flare. From these parameters the electron density and modal interference minima profiles will be constructed. The unperturbed and perturbed conditions of the profiles will be compared. It has been found that there is a relationship between the X-ray solar flux and VLF data for a solar flare. An attempt will also be made to see if there is any relationship between the July 2007 to May 2008 X-ray solar flux and VLF data.

1.2 History of detection methods

Bain and Hammond (1975) compared different methods of using ground techniques of detecting solar flares. At the time observations of LF (Low Frequency) phase height changes were thought to be the most efficient way of monitoring solar flares and were observed with 13% of optical solar flares. When VLF data were compared with optical flares listed in the *Solar Geophysical Data*, it showed that 18% of all solar flares are associated with Sudden Phase Anomalys (SPAs) but if only flares of high X-ray flux were considered, 35% were found to be associated with phase height changes. Only the part of VLF data between sunrise and sunset were considered since solar flares only occur on the dayside of the Earth, arriving within a few seconds. It proved that observing SPAs rather

than sudden height changes would be more efficient for detecting solar flares. A conclusion was made looking at X-ray solar flares in the 0.05–0.3 nm band that were accompanied by SPAs for the period of January 1969 to December 1970 that the percentage:

- increases with the measured peak X-ray flux of the solar flare,
- decreases progressively with increasing solar zenith angle (the angle between the zenith and the Sun), χ, when this angle exceeds about 60°,
- is 100% for solar flares of peak flux greater than 6×10^{-7}J m^{-2} s^{-1} in the band occurring when $\chi < 60°$.

1.3 Rates and coefficients determined from chemical models

Models have been developed to understand the chemical processes involved in the D-region during a solar flare. These models take as input X-ray flux together with electron density data to compute the ionisation rates with the associated chemical changes as expected in a coupled atmospheric chemistry model.

Such a model was developed by Zinn et al. (1990) who made use of measurements from the Arecibo incoherent scatter radar and X-ray flux data from the GOES-2 and ISEE-3 satellites during a X-class solar flare that occurred on 18 August 1979. The model used was an extension of one previously described by Zinn et al. (1982).

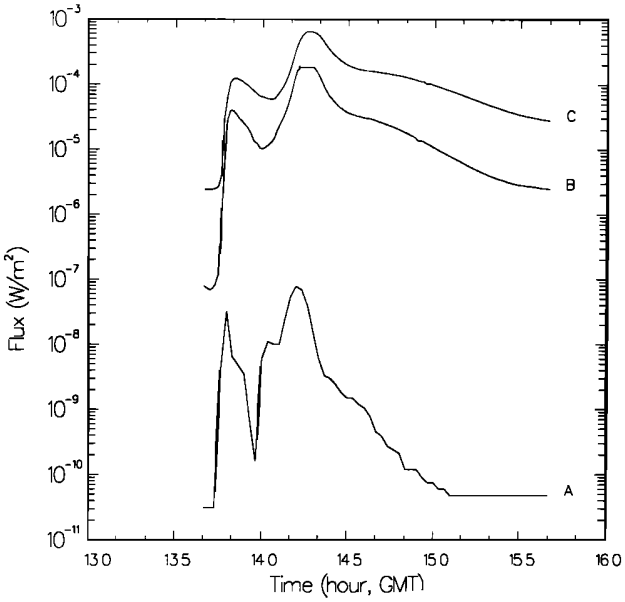

Figure 1.1: Solar X-ray flux data from GOES 2 and ISEE 3 satellites. Curve A: 0.029–0.048 nm; curve B: 0.05–0.4 nm; curve C: 0.1–0.8 nm (Zinn et al., 1990).

Specifically from the model, photochemical and photoelectron-collision rate coefficients

were computed as functions of altitude and time based on the time-varying solar output spectrum and solar zenith angle and the varying column densities of absorbers. The model was adjusted specifically for the D-region reactions and species.

The observed solar X-ray flux in the different bands from GOES-2 and ISEE-3 is given by Figure 1.1. During the period that the solar flare occurred, the electron densities for the D-region were measured. From the measured X-ray flux the ionisation rates were computed and the results are shown in Figure 1.2. The computed electron densities, shown in Figure 1.3, compared well with the measured electron densities (Figure 1.4) which suggests that the Zinn et al. (1990) model includes the most important chemical reactions.

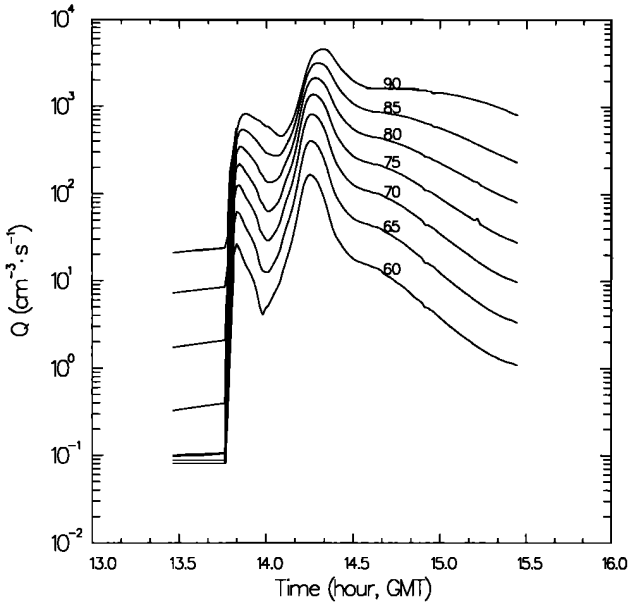

Figure 1.2: Contours of computed ion-pair production rates before and during the solar flare, at altitudes between 60 and 90 km (Zinn et al., 1990).

1.4 Wait's parameters

The D-region is sometimes characterised using Wait's parameters, H' (a measure of the reflection altitude in km) and β (a measure of the sharpness or rate of change of electron density with height). More specifically they are used to determine the height profile of conductivity parameter

$$\omega_r(z) = 2.5 \times 10^5 \cdot \exp[\beta(z - H')] \ \text{(rad/sec)} \tag{1.1}$$

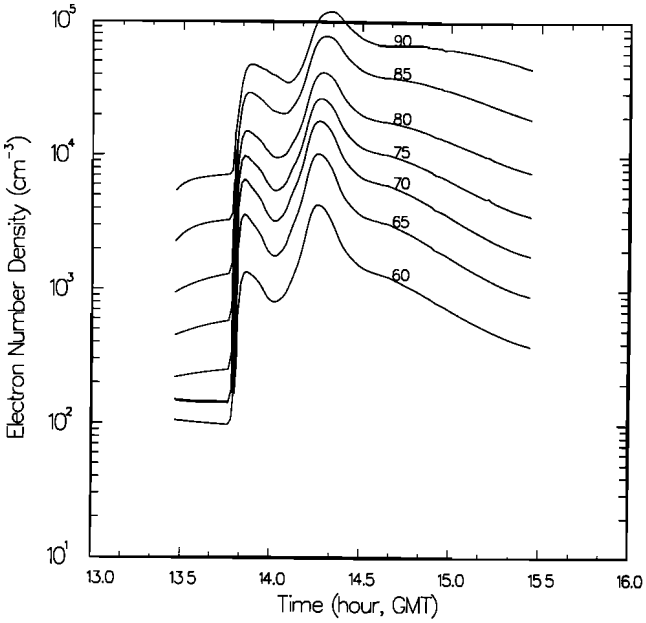

Figure 1.3: Computed electron concentrations before and during the solar flare, at the indicated altitudes (Zinn et al., 1990).

based on the model described by Wait and Spies (1964) and the exponential electron density model (Wait, 1962; Thomson, 1993)

$$N_e(z, H', \beta) = 1.43 \times 10^{13} \cdot \exp(-0.15H')\exp[(\beta - 0.15)(z - H')] \text{ (electrons/cm}^3\text{)}. \quad (1.2)$$

The electron density height profiles are presented for $H' = 75$ km (Figure 1.5) and $\beta = 0.3$ km^{-1} (Figure 1.6). Figure 1.5 shows how the gradient of the electron density profile increases as β increases for $H' = 75$ km. From Figure 1.6 one sees that the gradient of the electron density profile remains unchanged but is shifted for different values of H'. This will prove to be useful in sections to follow when discussing the effects of solar flares on the D-region.

1.5 Characterising D-region enhancements by VLF observations

McRae and Thomson (2004) made use of VLF observations together with Wait's parameters to characterise the D-region. The unperturbed day-time propagation paths' amplitude and phase were modelled by making use of the NOSC computer programs (MODESRCH, MODEFNDR, LWPC). The lengths of the propagation paths were in the

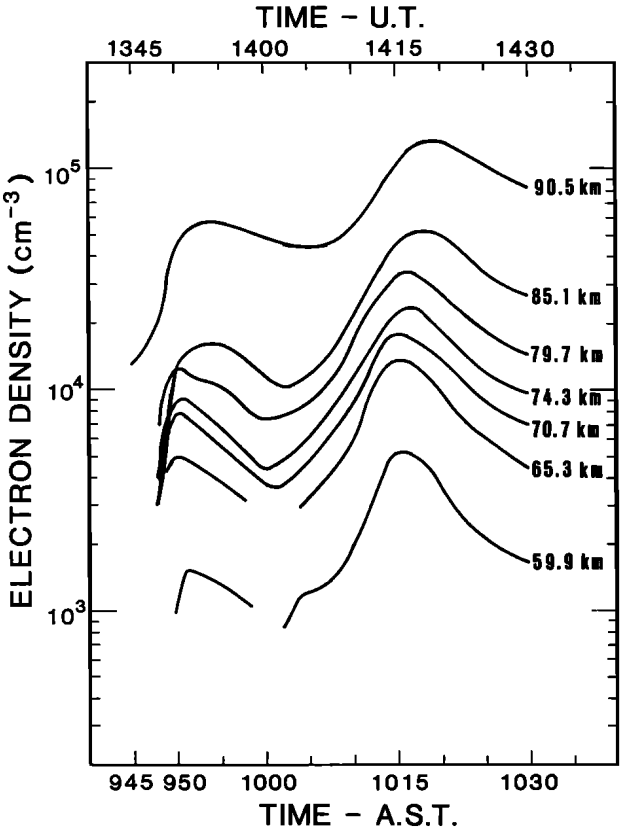

Figure 1.4: Measured values of electron densities as functions of time for several altitudes (Zinn et al., 1990).

order of 8.1–12.3 Mm and the frequency range was 10.2–24.8 kHz. All the paths were predominantly over the ocean.

The results that they found were that the amplitude and phase of the VLF signal depended on the size of the solar flare as well as on the exact state of the ionosphere before and during the flare. Their results also showed that the effect of the solar flare was somewhat dependent on the solar zenith angle. For their series of transmitters they found that there is a clear decrease in amplitude with X-ray flux at the lower VLF frequencies, especially for the west-to-east paths. For higher frequencies the decrease in amplitude tends to zero and for even higher frequencies such as from 21.4 kHz the amplitude increases with solar flare flux. For all the transmitter paths they found that the phase advances at the receiver with increasing solar flux.

Using Long Wave Propagation Code (LWPC), McRae and Thomson (2004) calculated H' and β. Knowing the transmitter locations, transmitting powers and the VLF amplitude and phase from observations they could vary H' and β until the calculated amplitude and phase matched those of the observations. It was found that H' decreased and β increased from the unperturbed conditions for a solar flare. The physical

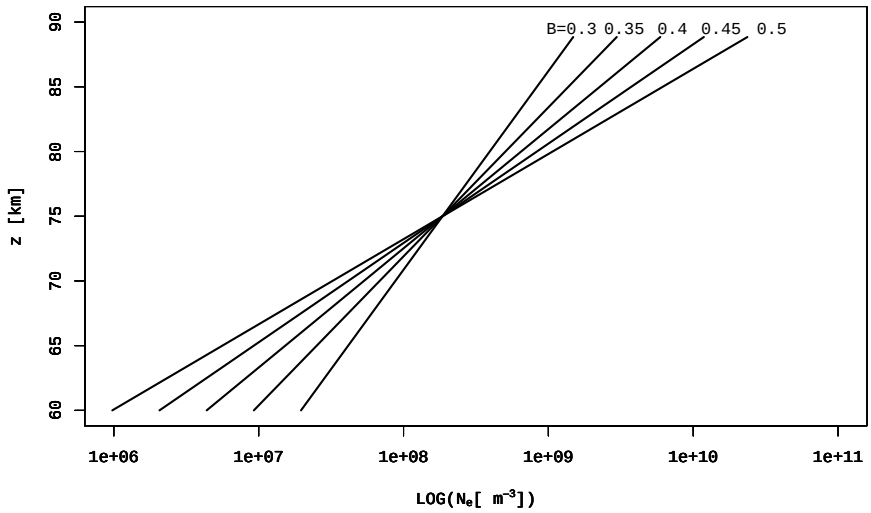

Figure 1.5: Electron density profiles for $H' = 75$ km.

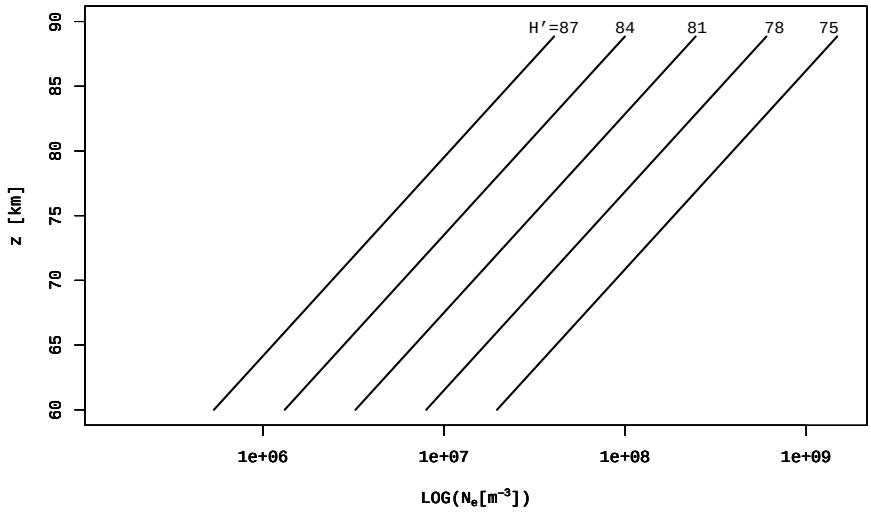

Figure 1.6: Electron density profiles for $\beta = 0.3\ \mathrm{km}^{-1}$.

explanation for this is that the increase of X-ray flux ionises the D-region further. The increase in ionisation lowers the reflection height of the D-region in proportion roughly to the logarithm of the X-ray flare intensity. For one of their paths they found that for an X5 flare H' lowered from 71 km to about 58 km.

The propagation model implemented in LWPC treats the space between the lower ionosphere and the Earth's surface as a waveguide. The upper boundary of the waveguide is the ionosphere which is characterised by a conductivity parameter (H'). A

horizontally homogeneous exponential conductivity profile was used throughout, described by H' and β. A change in H' an β would lead to a modification in the waveguide, leading to a change in the amplitude and phase of the signal. LWPC also has a mode-searching algorithm and therefore is able to calculate the contribution of all the modes at the receiver. For a specified H' and β, LWPC calculates how the signal varies with distance from the transmitter. It is also possible to compute the amplitute and phase at a specific location. The user is then able to vary H' and β until the result in the change of the amplitude and phase calculated by LWPC matches that of the observations. Using this method the user is able to calculate the change in H' and β.

The user will have to make some assumptions about the unperturbed values for H' and β. NOSC have recommended $H' = 72$–74 km and $\beta = 0.3\ \mathrm{km}^{-1}$ for winter mid-latitude. They did not however include recommendations for variation of H' and β with solar zenith angle (Morfitt, 1977).

The assumptions that are made using LWPC in all the cases is to assume an exponentially varying ionosphere and that H' and β pertain along the propagation path. The latter ignores the fact that H' and β does not vary with solar zenith angle and LWPC takes the Sun to be directly overhead. On short north-south propagation paths, where the Sun is in the middle of the path the assumption may be considered as good. If the propagation paths are west-east it will mean that H' and β will vary along the path. For example if the Sun is almost in the middle of a long west-east propagation path the waves would propagate in a waveguide that is broader in the middle and narrower at the ends. LWPC can't simulate this scenario where H' and β change along a propagation path.

Sometimes an increase in amplitude at certain receivers is observed and can be described by the interference of several modes. All the different modes contribute to the signal. The complexity of calculating H' increases when more modes are considered by LWPC.

The change in amplitude is found to be more sensitive to β than H' when using LWPC to match the measured values. This is because β affects the attenuation of the waves. In the case where H' is calculated to be lower than expected by LWPC to match the amplitude, Thomson (1993) suggest that there were modes excited along the propagation path. A phase advance for a signal is also found to be more sensitive to H' than β.

1.5.1 LWPC capabilities and model constraints

Previous stated a simple horizontally homogeneous exponential conductivity profile was choosed but one can also specify a complicated spatially varying distributions of electron and charged-ion densities.

The defualt model of the ionosphere used in LWPC employs a conductivity that increases exponentially with height. A log-linear slope and reference height define this exponential model. The defualt model defines an average value of the slope and reference height that depends on frequency and diurnal condition. This model was derived from extensive analysis of available measurements as described by Ferguson and Snyder (1980), Ferguson (1992) and Morfitt (1977). The defualt model of the lower boundary of the waveguide is based on the Westinghouse Geophysics Laboratory conductivity map (R., 1968).

Propagation paths are broken into a series of horizontally homogeneous segments. The distribution and the parameters of the segments are determined by changes in the ionosphere, ground conductivity and the geomagnetic field. Segments with a common ground conductivity and ionosphere are grouped together and processed in order of increasing distance from the transmitter. At the beginning of each of these groups, a mode-searching algorithm is used to obtain starting solutions. The mode solutions in the remaining segments of a particular group are obtained by extrapolating up to three sets of existing solutions by using distance from the transmitter as the extrapolation variable. The extrapolated solutions are adjusted for the effects of the geomagnetic field.

The transision between the daytime and nighttime ionosphere is specified in such a way so that the daytime ionosphere is specified for solar zenith angles less than 90° and the nighttime ionosphere for solar zenith angles greater than 99°. The model of the ionosphere used by LWPC produces an exponential increase in conductivity with height specified by a slope, β, in $\mathrm{km}^{-1}$and reference height, H', in km. Values for β and H' are specified by the program for both daytime and nighttime at each of two referece frequencies. Given the frequency specified by the user, values of β and H' for day and night are obtained by linear interpolation in frequency. Between the daytime and nighttime values of β and H', five additional values of β and H' are calculated at equal intervals.

An example of a LWPC input file is given in Appendix A.

1.6 Extrapolating X-ray flux data from GOES using VLF data

On 4 November 2003, the largest flare observed by the GOES satellites was recorded. The magnitude of the X-ray flare must have been greater than X28 ($2.8\,\mathrm{mW/m^2}$) and

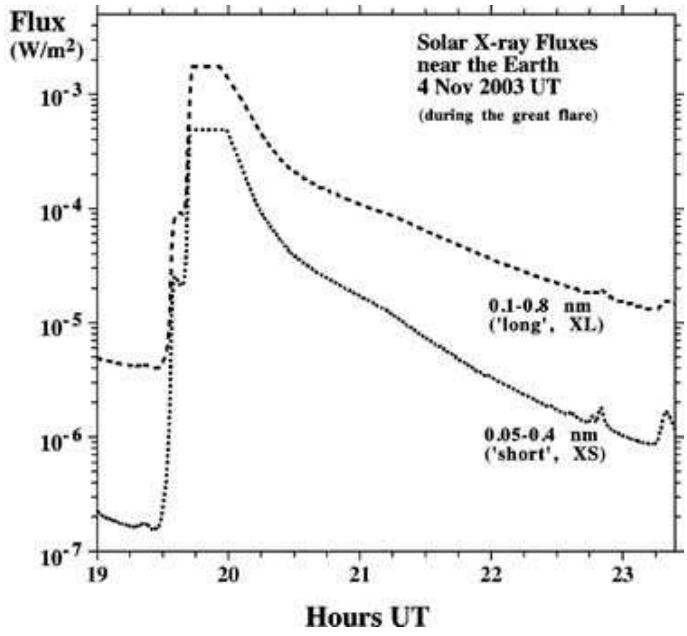

Figure 1.7: X-ray fluxes measured on GOES-12 during the great solar flare of 4 November 2003 (Thomson et al., 2004).

saturated the GOES detectors. Because the detectors were saturated, the true magnitude of the flare could not be determined from the GOES readings. The profiles of the flare recorded by the GOES detectors in the 0.1–0.8 nm and 0.05–0.4 nm band are given in Figure 1.7.

One way of trying to properly classifying the event was by using a ground based technique. Thomson et al. (2004) made use of VLF observations to extrapolate the X-ray flux and thus giving what would hopefully be a better classification of the flare. They used several transmitter paths from US Navy transmitters across the Pacific Ocean to Dunedin, New Zealand. These paths can be seen in Figure 1.8.

It was found that the VLF phase data scaled the unsaturated logarithm of the flux data linearly. The VLF data was then extrapolated also for the period for which the GOES detectors were saturated. After extrapolating the data, it emerged that the X-ray solar flare should have been classified as a X45 solar flare rather than X28. The results are shown in Figures 1.9 (a) and (b). Because the phase data follows the X-ray flux data it suggests that the X-ray flux is responsible for the ionisation of the D-region during the time of the solar flare and being the dominant source of ionisation, decreasing the reference height and therefore advancing the phase at the receiver. The timescale of the change in the phase also compares well with the timescale of the flux.

Using the same technique, Thomson et al. (2004) scaled the flux data of a X-ray solar flare that did not go beyond the saturation level of the GOES detectors, a class X10

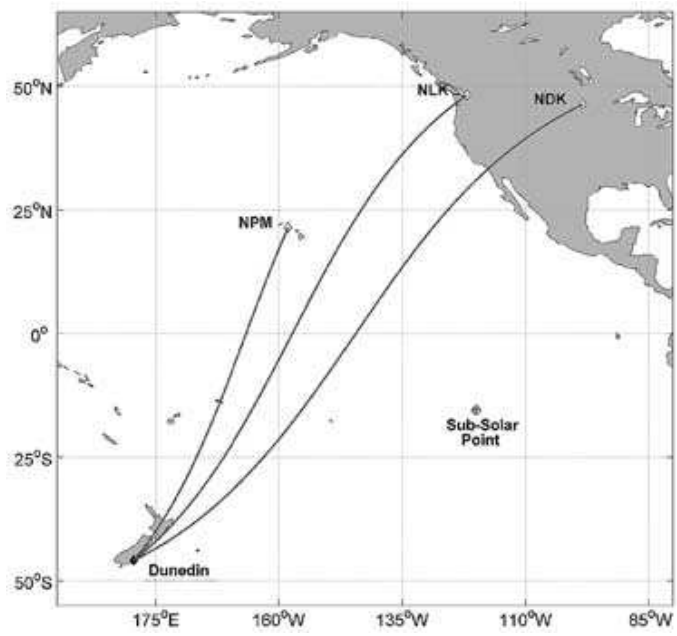

Figure 1.8: The VLF radio paths used to measure the flare (Thomson et al., 2004).

solar flare. It was found that the VLF data tracked the flux data well, including the peak of the flux data (see Figure 1.10). This gave some confidence for the extrapolation of the data that saturated the GOES detectors for the large flares.

1.7 Classifying X-ray solar flares by looking at perturbations in electron density profile

Following on the work of McRae and Thomson (2004), Grubor et al. (2008) made use of Wait's parameters to describe the state of the ionosphere on quiet days and during a solar flare. A more detailed study was done on how solar flares would affect the D-region as a function of increasing X-ray flux.

Using the LWPC code, H' and β were calculated and used to determine the exponential electron density model in (1.2). This was done by Grubor et al. (2008) for intervals from $z = 60$ km to 90 km where both the perturbed and unperturbed ionospheric electron densities were compared (see Figure 1.11). The unperturbed electron density on a quiet day at a specific time for a propagation path was found to have an increase of 10^7 m^{-3} at a height of 60 km to about 10^9 m^{-3} at the upper boundary of the D-region (about 90 km). The increase of X-ray flux from the flare on 12 July 2005 lowered the altitude where the electron density of 10^9 m^{-3} occurred by 13 km. Also, they determined where on the transmitter path an ionospheric modification would result in the maximum VLF

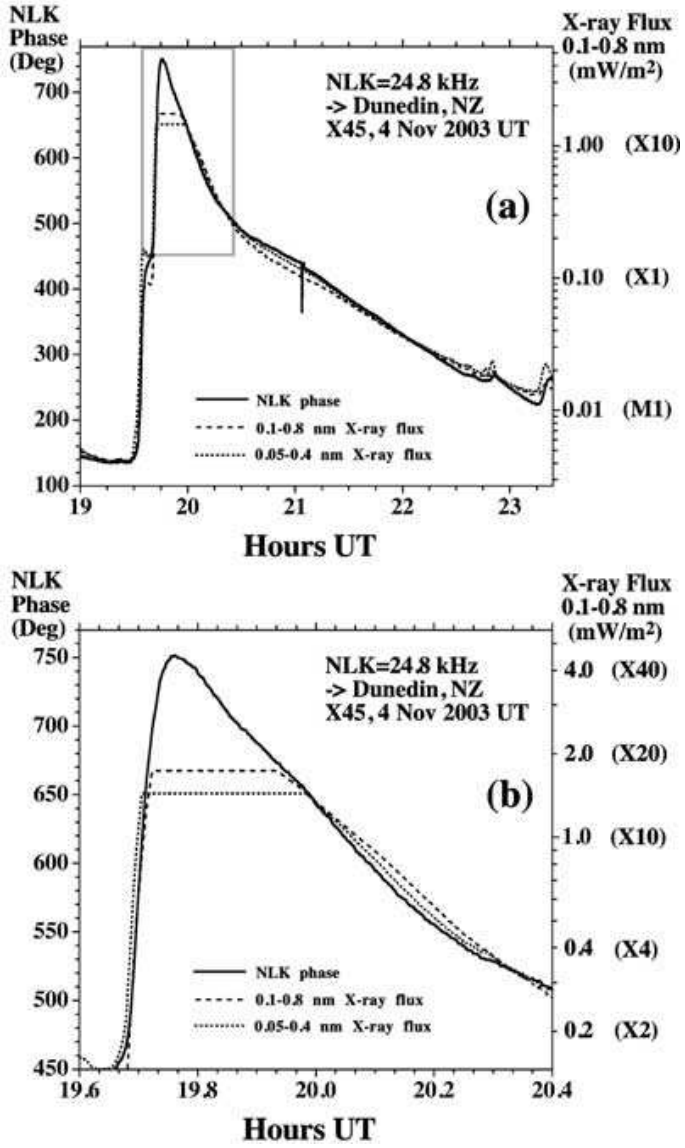

Figure 1.9: (a) The phase of NLK, Seattle, as received at Dunedin, NZ, during the great flare on 4 November 2003, compared with the GOES X-ray fluxes from Figure 1.7. (b) Close-up of the plots near the peak, in the box in (a) (Thomson et al., 2004).

perterbation. It emerged that this occurred at the main modal minimum which was located around 750 km from the source (see Figure 1.12).

It was found that solar flares starting from class C1–C2 would be detectable by using VLF observations. Assuming minimum modal interference at the location where the observations were made, more intense solar flares increased the effect on the amplitude and phase of the signal and lowers the reflection height further.

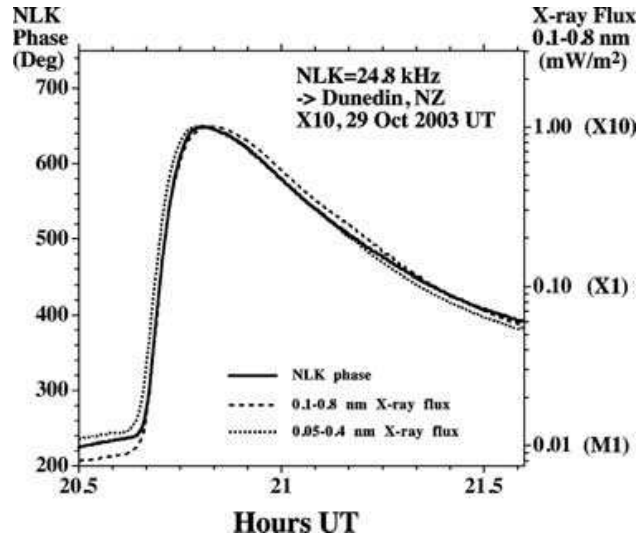

Figure 1.10: The phase of NLK, Seattle, as received at Dunedin, NZ, during the X10 flare of 29 October 2003 compared with X-ray fluxes from GOES detectors (Thomson et al., 2004).

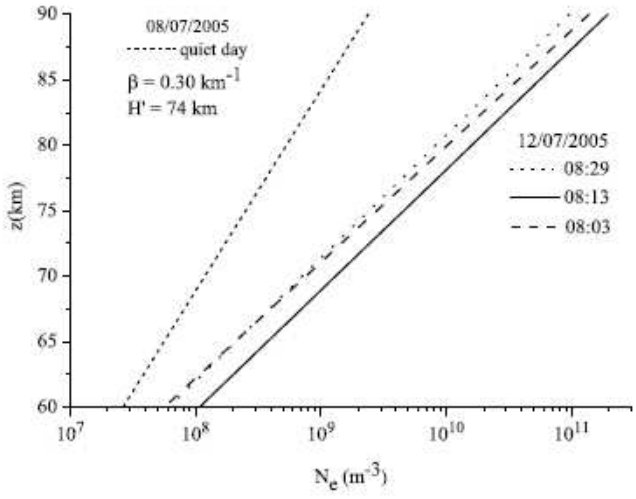

Figure 1.11: Changes in the electron density profile on 12 July 2005 in the course of the C7.5 flare derived from the phase and amplitude variation (Grubor et al., 2008).

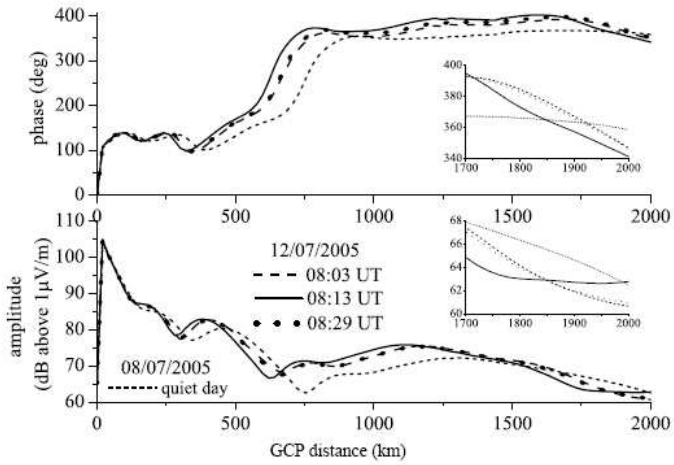

Figure 1.12: Variation of phase and amplitude of the GQD signal along the GCP from Skelton to Belgrade, calculated for three characteristic times during the C7.5 event on 12 July 2005. (Grubor et al., 2008).

Chapter 2

GOES and VLF data

The GOES satellites consist out of a constellation of satellites that are all in geostationary orbits. The X-ray telescope on the GOES satellite measures in real-time solar X-ray flux in the spectral range of 0.05–0.4 nm (short sun channel) and 0.1–0.8 nm (long sun channel). X-rays are detected by two ion chambers, one for each spectral range. The detector output signals are processed by separate electronic channels that provide automatic range selection. Nominal flux levels expected are on the order of 2×10^{-8} to 2×10^{-3} W/m^2 for the long channel and 5×10^{-9} to 5×10^{-4} W/m^2 for the short channel. The sampling rate of the X-ray flux was once every 0.512 seconds. The 1 minute averaged GOES data was used for the data analysis that will follow in a later section.

The transmitters transmitted minimum shift keying modulation (MSK). The software system, UltraMSK, analyses the MSK signals and keeps track of their amplitude and phase. The algorithm is yet to be published and a brief description of the the algorithm is quoted from one of the developers (James Brundell, james@brundell.co.nz): " The broadband VLF signal is mixed with in-phase and quadrature phase components of a local oscillator running at the same frequency as the transmitter. The resulting in-phase and quadrature-phase baseband waveforms are then low pass filtered. Next the MSK bit clock is recovered and the signal is integrated over one bit period. The receiver incorporates a post-demodulation clipping algorithm to reduce the effect of large amplitude lightning generated impulses. The key aspect is the quadrature phase mixing that produces the signal phasor from which the signal amplitude and phase is measured once the MSK signal is demodulated. In UltraMSK, the receiver uses the precise 1 Pulse Per Second (PPS) signal from a GPS receiver to synthesize any required reference frequencies for the local oscillator etc."

The VLF data was gathered by the Space Research Group, European Union, Budapest, P.O. Box 32 H-1518, Hungary. They were courtesy of Dr. Janos Lichtenberger.

Chapter 3

Wave guide theory

Consider waves propagating down a waveguide of arbitrary shape (Figure 3.1). Because the waveguide boundaries are considered to be a perfect conductor, the transverse electric and normal magnetic components on the walls are equal to 0, so the boundary conditions are

$$E^{\parallel} = 0, \tag{3.1a}$$

$$B^{\perp} = 0. \tag{3.1b}$$

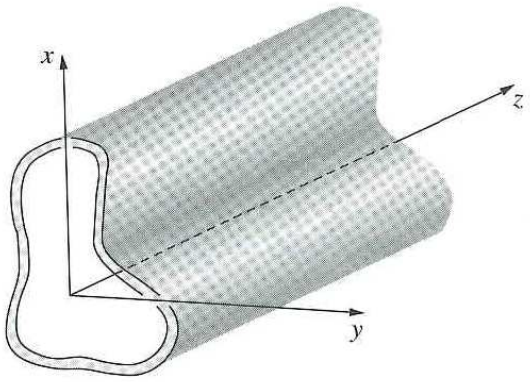

Figure 3.1: A waveguide having an arbitrary shape where propagation takes place in the z-direction (Griffiths, 1999).

Free charges and currents will be assumed to be induced on the surfaces of the plates in such a way as to enforce these constraints. The waves that are of interest are monochromatic waves propagating down the waveguide (in the positive z direction) where $\mathbf{E}$ and $\mathbf{B}$ have the form

$$\mathbf{E}(x, y, z, t) = \mathbf{E}_0(x, y)e^{i(kz-\omega t)}, \tag{3.2a}$$

$$\mathbf{B}(x,y,z,t) = \mathbf{B}_0(x,y)e^{i(kz-\omega t)}, \tag{3.2b}$$

where k is the wavenumber for a wave travelling in the z direction. Only the parts where k is real will be considered. It is essential that these waves satisfy Maxwell's equations in the waveguide:

$$\nabla\cdot\mathbf{E} = 0, \tag{3.3a}$$

$$\nabla\cdot\mathbf{B} = 0, \tag{3.3b}$$

$$\nabla\times\mathbf{E} = -\frac{\partial\mathbf{B}}{\partial t}, \tag{3.3c}$$

$$\nabla\times\mathbf{B} = \frac{1}{c^2}\frac{\partial\mathbf{E}}{\partial t}. \tag{3.3d}$$

One now has to find functions of $\mathbf{E}_0$ and $\mathbf{B}_0$ such that the fields in (3.2) obey (3.3) and the boundary conditions (3.1). Consider the components of the wave:

$$\mathbf{E}_0 = E_x\hat{\mathbf{x}} + E_y\hat{\mathbf{y}} + E_z\hat{\mathbf{z}}, \tag{3.4a}$$

$$\mathbf{B}_0 = B_x\hat{\mathbf{x}} + B_y\hat{\mathbf{y}} + B_z\hat{\mathbf{z}}. \tag{3.4b}$$

where each of the components is a function of x and y. Putting equations (3.4) into equations (3.3c) and (3.3d), and solving for E_x, E_y, B_x and B_y the following equations are obtained:

$$E_x = \frac{i}{(\omega/c)^2-k^2}\left(k\frac{\partial E_z}{\partial x} + \omega\frac{\partial B_z}{\partial y}\right), \tag{3.5a}$$

$$E_y = \frac{i}{(\omega/c)^2-k^2}\left(k\frac{\partial E_z}{\partial y} - \omega\frac{\partial B_z}{\partial x}\right), \tag{3.5b}$$

$$B_x = \frac{i}{(\omega/c)^2-k^2}\left(k\frac{\partial B_z}{\partial x} - \frac{\omega}{c^2}\frac{\partial E_z}{\partial y}\right), \tag{3.5c}$$

$$B_y = \frac{i}{(\omega/c)^2-k^2}\left(k\frac{\partial B_z}{\partial y} + \frac{\omega}{c^2}\frac{\partial E_z}{\partial x}\right). \tag{3.5d}$$

Once the longitudinal components, E_z and B_z, are determined the other components can easily be obtained just by differentiating. Finally, (3.5) is inserted into equations (3.3a) and (3.3b) to obtain the uncoupled for E_z and B_z:

$$\left[\frac{\partial^2}{\partial x^2} + \frac{\partial^2}{\partial y^2} + k_0^2 - k^2\right]E_z = 0, \tag{3.6a}$$

$$\left[\frac{\partial^2}{\partial x^2} + \frac{\partial^2}{\partial y^2} + k_0^2 - k^2\right]B_z = 0. \tag{3.6b}$$

where ω/c is replaced by the free space wavenumber k_0. Rewriting equation (3.6) in compact format for the electric field

$$(\nabla_\perp^2 + k_0^2 - k^2)E_z = 0. \tag{3.7}$$

Similarly, for the magnetic field

$$(\nabla_\perp^2 + k_0^2 - k^2)B_z = 0. \tag{3.8}$$

The different modes of propagation will now be defined. For the transverse electric (TE) mode the electric field is transverse to the direction of propagation along the waveguide, $E_z = 0$. In the transverse magnetic (TM) mode the magnetic field is perpendicular to the direction of propagation, $B_z = B_x = 0$. In the transverse electromagnetic (TEM) mode both the electric and magnetic fields are normal to the direction of propagation, $E_z = 0$ and $B_z = 0$.

Consider the TM mode (Eyges, 1972; Lorrain et al., 1988). Equation (3.7) would be the complete equation for describing the longitudinal components in a rectangular waveguide with internal dimensions $x \in [0, a]$ and $y \in [0, b]$ where k_0 is known for a given ω but the guide wavenumber, k, is unknown.

3.1 Horizontal parallel plate waveguide

Consider a parallel plate waveguide of perfect conducting planes and where the walls in the y direction extent to infinity. For a wave incident on a conducting plane at an angle θ to the normal (Figure 3.2), with wave vector

$$\mathbf{k} = (-\cos\theta\hat{\mathbf{i}} + \sin\theta\hat{\mathbf{k}}) \tag{3.9}$$

and electric field described by

$$\mathbf{E}_i = E_i e^{k_0 j(-x\cos\theta + z\sin\theta)}\hat{\mathbf{j}}. \tag{3.10}$$

The reflected wave has electric field

$$\mathbf{E}_r = E_r e^{k_0 j(x\cos\theta + z\sin\theta)}\hat{\mathbf{j}} \tag{3.11}$$

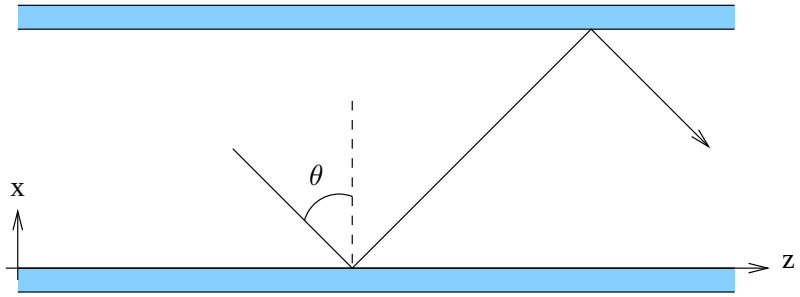

Figure 3.2: A ray propagating along a parallel plate waveguide.

The tangential component of the electric field on the conductor is zero so that $\mathbf{E}_i = -\mathbf{E}_r$. The total field is thus

$$\mathbf{E} = -2jE\sin(k_0 x\cos\theta)e^{k_0 jz\sin\theta}\hat{\mathbf{j}} \tag{3.12}$$

where the sin factor results from interference between the incident and reflected waves.

The last factor in (3.12) is the spatial portion of a wave travelling in the z direction with wave number

$$k = k_0\sin\theta = \frac{2\pi}{\lambda}. \tag{3.13}$$

The guide wavelength is related to that in free space by

$$\lambda = \frac{\lambda_0}{\sin\theta}, \tag{3.14}$$

so that $\lambda \geq \lambda_0$.

The other spatially variable factor in 3.12, $\sin(k_0 x\cos\theta)$, indicates that this is not a conventional plane wave with constant amplitude on any plane perpendicular to the propagation direction.

The presence of a second conducting plane at $x = a$ imposes a second boundary condition,

$$\sin(k_0 a\cos\theta) = 0 \tag{3.15}$$

which is satisfied if

$$k_0\cos\theta = \frac{m\pi}{a} \text{ for } m = 1, 2, 3, \cdot \tag{3.16}$$

Subject to this condition, (3.12) describes a wave propagating in a parallel plate waveguide.

For a waveguide of infinite walls one also has in addition to (3.8):

$$\frac{\partial}{\partial y} = 0$$

so that

$$\frac{\partial^2 E_z}{\partial x^2} + (k_0^2 - k^2)E_z = 0. \tag{3.17}$$

Equation (3.17) has sinusoidal solutions if $k_0^2 - k^2 > 0$. This is equivalent to $\lambda > \lambda_0$, meaning that the wavelength along the waveguide is longer than the wavelength of the plane wave. Equation (3.17) has the solution

$$E_z = E \sin k_x x \tag{3.18}$$

where

$$k_x = \frac{m\pi}{a} \text{ for } m = 1, 2, 3, \cdots$$

This solution is called the TM_m mode. The other components for the TM mode may be derived using equation (3.5):

$$E_x = \frac{ik}{k_x} E \cos k_x x, \tag{3.19}$$

$$B_y = \frac{iw}{k_x c^2} E \cos k_x x. \tag{3.20}$$

One can also write

$$k^2 = k_0^2 - k_x^2 = k_0^2 - \frac{\pi^2 m^2}{a^2}. \tag{3.21}$$

so that

$$k = \sqrt{k_0^2 - \frac{\pi^2 m^2}{a^2}} \tag{3.22}$$

If

$$k_0^2 < \frac{\pi^2 m^2}{a^2} \equiv k_m^2, \tag{3.23}$$

the wavenumber is imaginary and the wave becomes evanescent. One can also write equation (3.23) in terms of frequency

$$\nu_m = \frac{mc}{2a} \tag{3.24}$$

where ν_m denotes the cutoff frequency for a given mode. Using (3.24) the guide wavenumber can be written as

$$k = k_0 \sqrt{1 - \frac{\nu_m^2}{\nu^2}}. \tag{3.25}$$

The lowest cutoff frequency for the waveguide will occur at the mode TM_1:

$$\nu_1 = \frac{c}{2a}. \tag{3.26}$$

It can also easily be shown that the E_z and B_z components for the TE_0 and TM_0 waves will be zero corresponding to the TEM wave as defined earlier.

Using (3.21) and (3.16) one can express the waveguide wavenumber as follows:

$$k = k_0 \sin\theta. \tag{3.27}$$

The phase velocity along the waveguide is

$$v_\phi = \nu\lambda = \frac{\omega}{k}. \tag{3.28}$$

Using equation (3.27) it can be written as

$$v_\phi = \frac{c}{\sin\theta} > c. \tag{3.29}$$

The group velocity, however, is given by

$$v_g = c \sin\theta, \tag{3.30}$$

and is less than the speed of light.

This concludes the derivation for the model of a parallel plate waveguide for the TM wave. A similar derivation can be made for the TE waves. This model can be adapted to describe the EIW where the waveguide consists of two horizontal parallel plates, in this case the upper boundary is the lower edge of the ionosphere and the lower boundary the surface of the Earth. The surface of the Earth (land and sea) and the lower edge of the ionosphere are assumed to be perfect conductors. The space between these plates is considered to be effectively a vacuum. From a communication perspective, considering the TE and TM waves as having different polarisations and propagating in the EIW, TM waves will be transmitted from vertical and TE waves from horizontal ground based antennas. TM waves are also known to be strongest near the surface of the Earth but become weaker with altitude. For TE waves, however, they are strongest at high altitudes, but are much weaker near the ground (Harrison, 1974). The waveguide that was discussed is a very simplistic view of waves propagating in the EIW. Some details are neglected:

(i) the curvature of the Earth and ionosphere,

(ii) the effects of the Earth's magnetic field,

(iii) effects of electron collisions, and

(iv) irregularities in the Earth-ionosphere waveguide.

3.2 Interpreting the different wave modes

To give some idea of what modes to expect propagating in the Earth-ionosphere waveguide, reference heights of $h_D = 75$ km for the daytime and $h_N = 88.5$ km for nightime will be used (Kikuchi, 1986). Considering the first modes of the TE and TM waves, that is TE_1 and TM_1, the cutoff frequencies can be calculated using equation (3.24) and the reference heights h_D and h_N. During daytime one would have:

$$\nu_{D1} = \frac{c}{2(75.0 \times 10^3 m)} \approx 2.0 \text{ kHz}, \tag{3.31}$$

and during the night:

$$\nu_{N1} = \frac{c}{2(88.8 \times 10^3 m)} \approx 1.7 \text{ kHz}. \tag{3.32}$$

This implies that only frequencies higher than these values for ν_{Dm} and ν_{Nm} will propagate, which is acceptable for the whole of the VLF spectrum (3–30 kHz). These frequencies, however, put some constraints on the ELF spectrum (3 Hz–3 kHz). Theoretically, depending on day or night, only those waves with frequencies 1.7–3.0 kHz will propagate in the waveguide when referring to the ELF range. This will mean that the majority of the waves for ELF will propagate in the TEM mode. Considering the transmitting frequency of 19.6 kHz that will be used in this thesis, the constraints can be defined on the order of modes that will contribute to the signal at the receiver. It can be showed that for $m = 9$ during the day, the driven frequency of 19.6 kHz is greater than the cutoff frequency of $\nu_{D9} \approx 18.0$ kHz. For modes greater than $m = 10$ ($\nu_{D10} \approx 20.0$ kHz) the waves will be evanescent. While 9 different modes may contribute to the signal, in most cases only the first few are considered because the attenuation rate of the higher-order modes are much greater than that of the lowest mode relative to θ for high values of m. When signals are transmitted over a long distance only the lowest mode is considered. Over short distances all propagating waves are considered since they all are comparable in amplitude (Davies, 1966).

3.3 Lightning, sferics and tweeks

The dominant source of Very Low Frequency (VLF) waves in the EIW is lightning discharges. When these discharges occur, a broadband spectrum of radiation is produced that propagates in the TM mode. If one neglects dispersion in the waveguide, all frequencies should arrive simultaneously at the receiver. When one constructs a spectrogram over a time series, one should find narrow vertical lines. These impulsive events are known as atmospherics or simply sferics. An example of a spectrogram showing only sferics is given by Figure 3.3.

From Figure 3.4 one can see “tweeks” occurring within the vertical narrow lines that are

produced. The "tweeks" are the delayed parts of a sferic in the spectrogram and are quantised for each sferic. These "tweeks" corresponds to the different frequency cutoffs for different modes that occur in the waveguide. Using (3.24) one can estimate a, which corresponds to the reflection height during that time of the day for a given mode m, or at least it gives a good estimation. One can also notice the delay of those frequencies that surround every "tweek" for the different modes. This can be explained by the group velocity v_g of waves, which is related to the guide wavenumber k, where the guide wavenumber is dependent on the cutoff frequency (see (3.23)). This implies that for waves in a given mode, with frequencies close to the cutoff frequencies, will have a slower group velocity and so will be delayed and the delay increases as the cutoff frequency is approached from above. A visual interpretation for the cutoff frequencies can be seen as waves where their nodes fall exactly on the boundaries of the surfaces of the waveguide. For $\theta = 90°$ it means that there will be no propagation for waves vertically down from the ionosphere to the surface of the Earth.

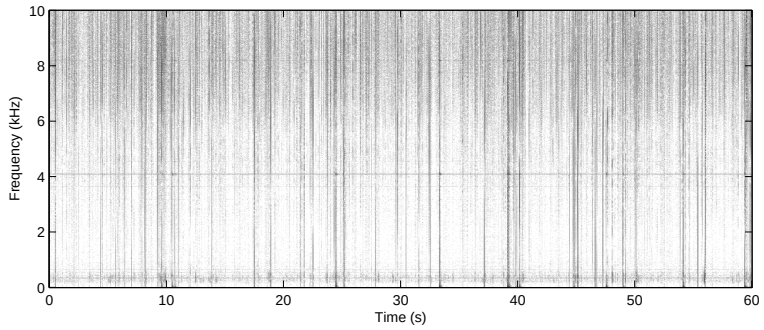

Figure 3.3: Broadband VLF spectrum showing sferics. Recorded at SANAE on 14 June 2009 at 18:20 UT.

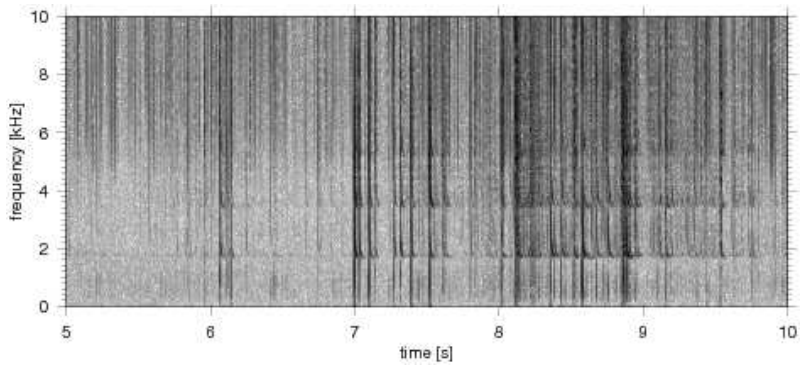

Figure 3.4: Broadband VLF spectrum showing sferics and tweeks. Recorded at Marion Island on 22 February 2003 at 21:00 UT.

As an exercise the reflection height can be calculated from the spectrum in Figure 3.4 using equation 3.24. For $m = 1$ the first "tweek" in the spectrum occurs around 1.8 kHz

so one has

$$1.8 \text{ kHz} = \frac{c}{2a}. \tag{3.33}$$

Solving for a the reflection height comes out to be 83.3 km. One can see from the spectrum that the "tweaks" are discreet. For example if $m = 2$ is considered it is shown at 3.6 kHz similarly giving a reflection height of 83.3 km.

Chapter 4

Terminator effects

4.1 Sunrise and sunset fadings

VLF transmitters are mainly used for navigation, location and timing. The waves produced by the transmitters travel over long distances and may be treated as propagating in the EIW. When VLF waves are transmitted from a vertical antenna, a number of modes are excited in the Earth-ionosphere waveguide. When only the first mode is considered, being predominant over a long distance, the electric field of the received signal is given by (Wait, 1962; Blackband, 1964) :

$$E = \frac{E_0}{h}|\Lambda_1| \exp(-\alpha_1 d) \times \exp\left[i\omega\left(t - \frac{d}{v_1}\right) + i \arg \Lambda_1\right] \tag{4.1}$$

where Λ_1 is the excitation factor for the first mode, α_1 is the attenuation rate of the first mode, v_1 is the phase velocity of the first order mode, d is the distance between the receiver and transmitter, t is the time, h is the reflection height, ω is the wave angular frequency and E_0 determines the radiation power. The arg component of the function extracts the angular component of its argument, i.e. $\arg\left(\mathrm{A}e^{i\theta}\right) = \theta$.

The diurnal profile of signal amplitude reproduces itself within a few consecutive days. A profile may contain many minima that occur for a specific time of the day for a given transmitter path. These usually occur around sunrise and sunset. Sunrise and sunset refers to the times where the terminator is seen in the region of the ionosphere of about 100 km altitude. This phenomena is known as sunrise or sunset fading. Where the EIW was considered to be sharply bounded by the D region, it in fact has horizontal gradients during disruptive periods such as near sunrise and sunset. These horizontal gradients lead to the creation of new modes at the discontinuity. One example of such a discontinuity is the terminator (where the night ionosphere meets the day ionosphere). The signal at the receiver will be a combination of many modes which may interfere

either constructively or destructively.

The successive signal minima when the terminator has moved a distance d is related to the first and second order mode phase velocities, v_1 and v_2 in the nighttime portion given by (Crombie, 1964, 1965):

$$d = \frac{v_1 v_2}{f(v_2 - v_1)}. \tag{4.2}$$

It has also been shown that the difference in attenuation rate between the second and first order modes can be determined from two successive pronounced variations $\triangle\phi$ and $\triangle\phi'$ observed during the signal amplitude fadings,

$$\tan \triangle\phi = \frac{E_2}{E_1} \quad \text{and} \tag{4.3}$$

$$\tan \triangle\phi' = d\frac{E_2'}{E_1'}. \tag{4.4}$$

Indices 1 and 2 once again correspond to the first and second order modes. E_1 and E_2 are the relative field strengths before the effect of the onset. E_1' corresponds to the first order mode and E_2' to the converted second-order mode after the onset effect. The difference in attenuation rates will be

$$\alpha_2 - \alpha_1 = 20 \left\{ \log \frac{E_2}{E_1} - \log \frac{E_2'}{E_1'} \right\} / d \tag{4.5}$$

where d is the distance moved by the terminator during the time interval between two successive phase deviations (corresponding to signal maxima). α_1 is the attenuation rate of the first mode and α_2 of the second mode.

Figure 4.1 (a) shows the attenuation rate, α_1, of the first order mode for a perfectly conducting Earth and an imperfectly reflecting ionosphere derived by Wait (1962). It shows that frequencies at the lower end of the VLF band are more attenuated during the day than at nightime, when the reference height is greater than during the day time. At frequencies around 20 kHz, attenuation rates for the first mode during daytime and nightime are similar (about 1.5 dB/Mm). The attenuation rates for the second order mode give a different picture as illustrated by Figure 4.1 (b). It is clear that the greater the frequency and the smaller the value for the reference height, the greater the attenuation will be for the second mode. At 20 kHz, the attenuation rate is about 3 dB/Mm for nightime ($H' \approx 87$ km) and to about 4.5 dB/Mm for daytime ($H' \approx 74$ km).

The excitation factor of the mth mode, Λ_m is defined as being a measure of the relative efficiency of launching a mode into the Earth-ionosphere waveguide (Wait, 1962). Figure 4.2 (a) shows that for higher frequencies and greater reflection heights the excitation of

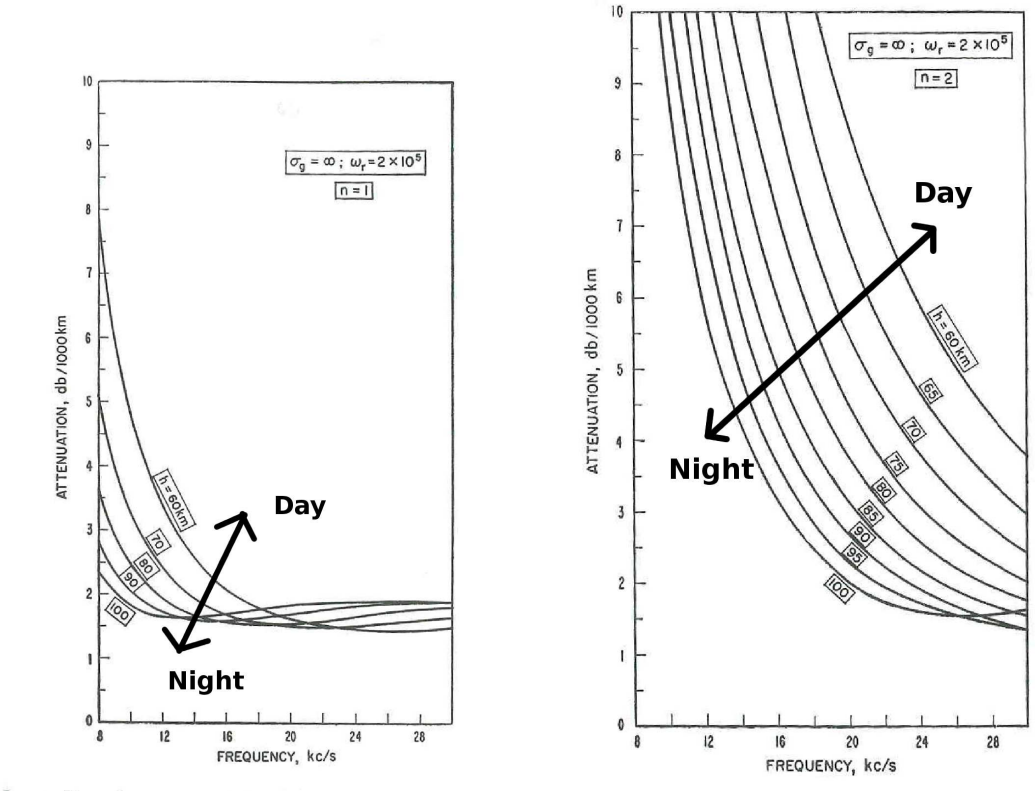

(a) (b)

Figure 4.1: Attenuation rate of the first (a) and second (b) mode for a perfectly conducting Earth and an imperfectly reflecting ionosphere (Wait, 1962).

the first mode becomes weaker. Figure 4.2 (b), also for a finite conducting Earth and ionosphere, shows the excitation factor for the second mode. Frequencies higher than 20 kHz and having heights greater than $H' = 80$ km experience a weak excitation of the second mode in the Earth-ionosphere waveguide. These definitions are important to get a feeling for the discussion to follow.

For a west-to-east transmission, where the sunrise terminator is located east of the transmitter and west of the receiver, a first and second-order mode is excited at the transmitter in the nightside waveguide and reaches the terminator, it does so with little attenuation. The night-time second-order mode then produces a first order mode at the terminator. The first-order mode that was produced propagates to the receiver, while the second-order mode itself suffers great attenuation in the dayside waveguide. This leads to interference that takes place at the receiver between the converted first-order mode at the terminator and the first-order mode from the transmitter. The interference results in sunrise fadings of the signal amplitude. The effects of mode conversion and mode interference are mostly evident at sunrise and on frequencies near and above 20 kHz. It is also known that mode conversion increases with increasing angle between the

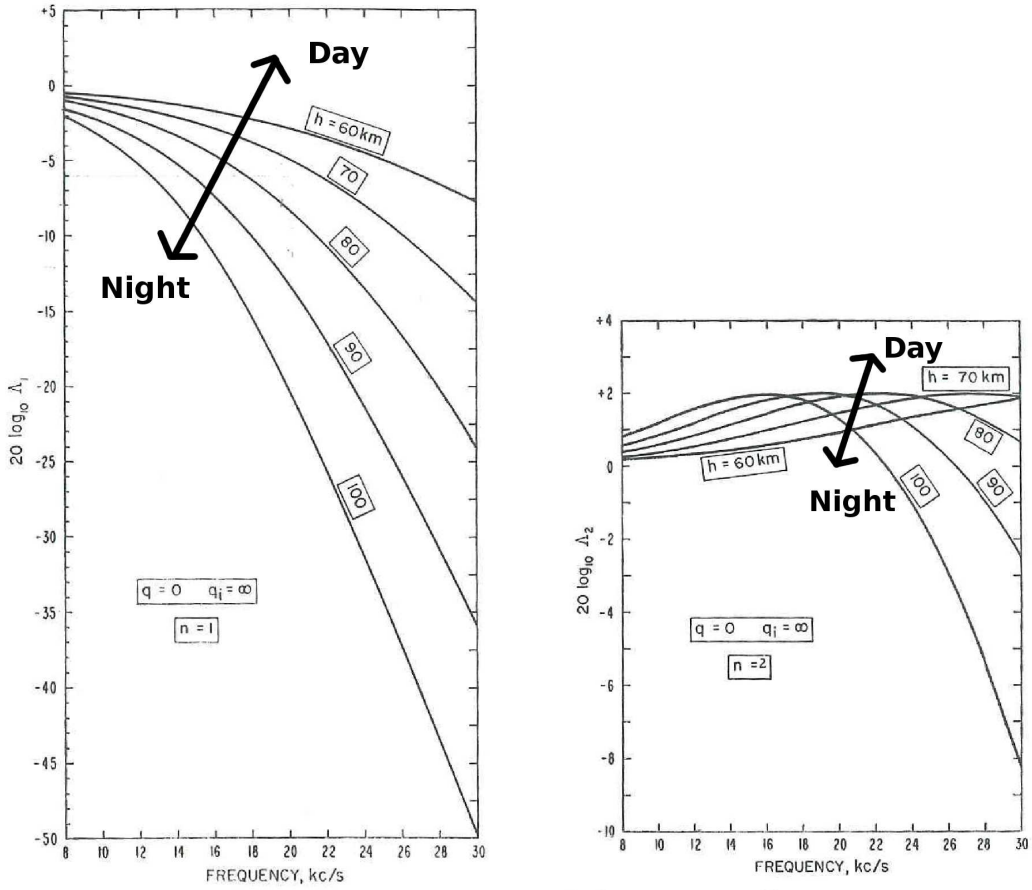

(a) (b)

Figure 4.2: Excitation factor of the first (a) and second (b) mode expressed in decibels for a finitely conducting ground and ionosphere (Wait, 1962).

path and terminator.

Figure 4.3 shows the setup for transmission paths between a selection of transmitters and a receiver in Budapest (47.3° N, 19.5° E). Note that all are west-to-east transmission paths. Table 4.1 gives the locations of the transmitters and the distance on the great circle path to the receiver. Figure 4.4 gives the average diurnal profile for four transmitters during north hemisphere autumn. All of the profiles contains minima at sunrise or sunset. For 19.6 kHz the effect of the interference between converted modes is less severe. However, there are clearly still minima occurring at sunrise and sunset. Comparing transmitters GBZ, ICV and FUO with NAA it is found that there is an increase in the number of minima at sunrise and sunset. This is consistent with (Kumar and Kumar, 2007) where it is expected for the number of minima to increase for signals travelling over greater distances. One can also see that the depth of the fadings at sunset is greater than at sunrise. This could be because the transmitter directly excites the interfering second order mode on the night-side of the path. During sunset the second

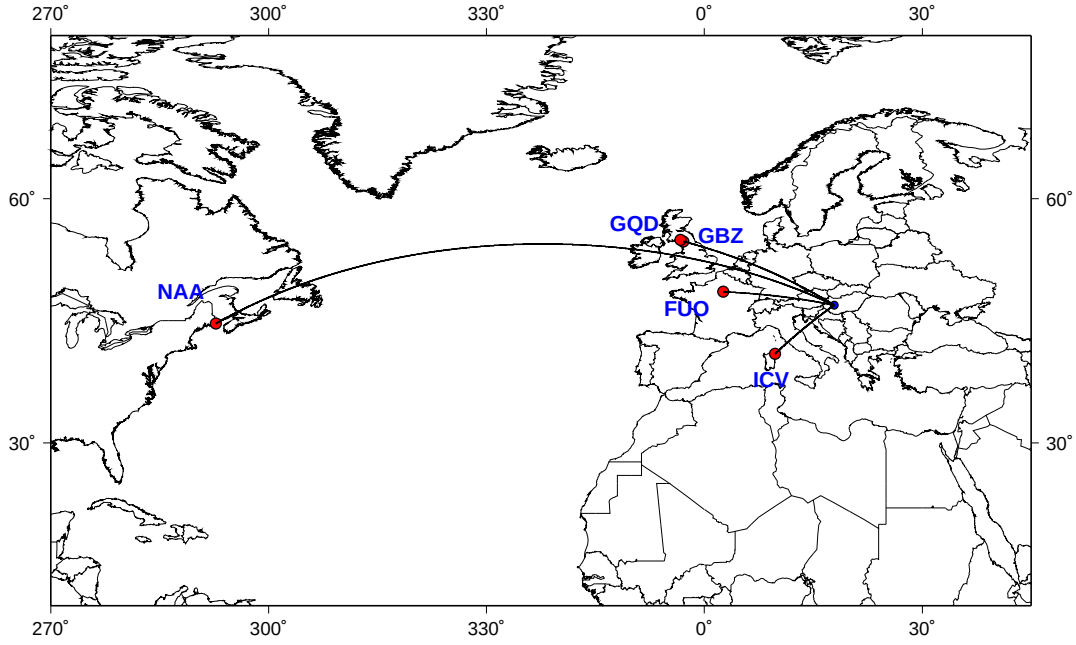

Figure 4.3: West-to-east transmission paths with receiver in Budapest.

order mode is created at the terminator. This could likely imply that there is a difference between the sunrise and sunset mode conversion efficiencies.

Mode conversion increases when the angle between the path and terminator increases. Cycle slippage (a phase change of exactly 360°, losing track of the phase) can occur when the modes are comparable in amplitude. Slippage can also occur when the phase varies very rapidly compared with the time constant of the receiver (Westerlund and Reder, 1970).

Table 4.1: Transmitter locations and GCP distances from transmitters to receiver in Budapest.

Transmitter	Frequency [kHz]	latitude	longitude	d [Mm]
GBZ	19.6	54.73° N	2.88° W	1.722
ICV	20.27	40.92° N	9.73° E	2.394
FUO	20.9	48.54° N	2.58° E	1.610
GQD	22.1	54.9° N	3.278° W	1.540
NAA	24.0	44.64° N	67.28° W	6.309

Figure 4.5 illustrates the change in the amplitude as the sun terminator crosses the receiver and transmitter. The terminator is simulated for the 15th September 2007, while the amplitude profile consists out of the average for the whole of September. Starting with Figure 4.5(a), as the sun rises and the terminator lies on the map between

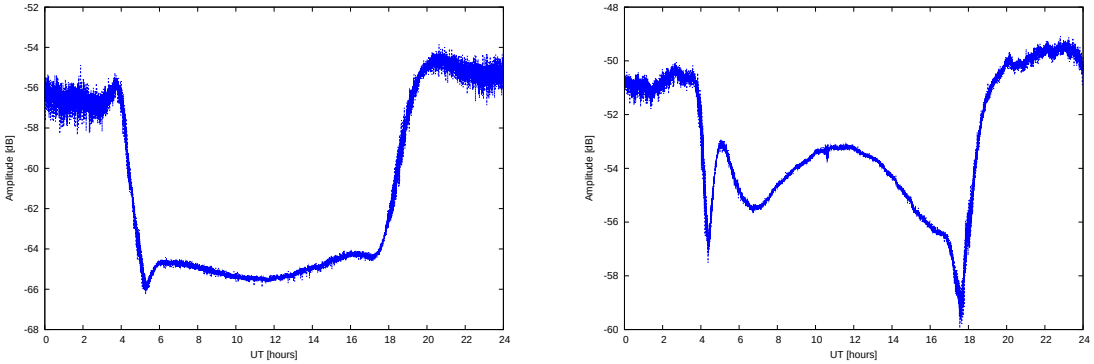

(a) 19.6 kHz

(b) 20.27 kHz

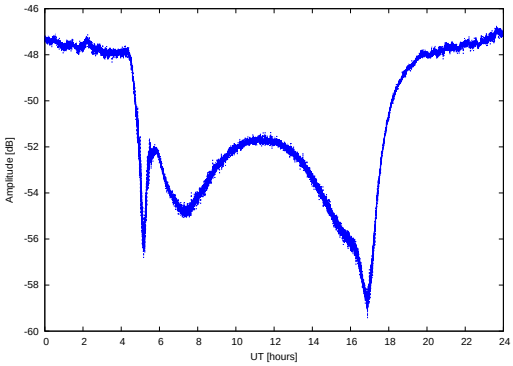

(c) 20.9 kHz

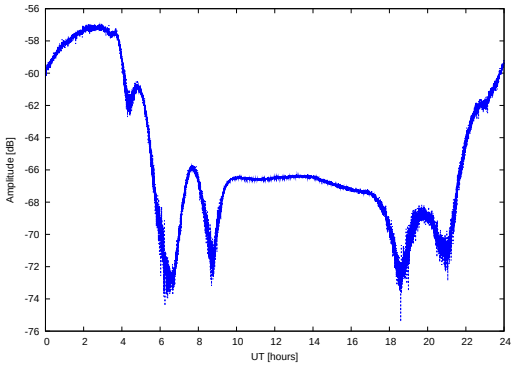

(d) 24.0 kHz

Figure 4.4: Comparison between different transmitter paths signal amplitude profiles: (a) GBZ. (b) ICV. (c) FUO. (d) NAA.

the transmitter and receiver, one can see that there is a sudden increase in the amplitude. At this stage (Figure 4.5(b)) there is interference between the first-order mode excited at the transmitter and the converted first-order mode that was originally excited as the second-order mode at the transmitter. The magnitude of the converted mode becomes comparable with the original first-order mode, contributing to the amplitude of the signal. After the terminator has crossed both the receiver and transmitter (Figure 4.5(c)), the first-order mode becomes predominant and is the main source contributing to the amplitude signal.

4.2 Monthly variation caused by terminator

The terminator effect has a well defined annual variation. During summer the sun rises earlier and the sun sets later than for winter. Figure 4.6 shows the change in the terminator profile across the transmitter paths. It is clear that the days during July are longer than those of January for the transmitter paths in northen hemisphere. This has a direct effect on the time when the atmosphere gets ionised and hence a modification in the waveguide

leading to a variation in the amplitude profile. Figure 4.7 illustrates this effect. Where one starts off with a very broad amplitude depression in summer, it narrows down during winter months being in the northen hemisphere.

As an exercise the amplitude change from day to night was calculated in a similar fashion to Kikuchi (1986) where the amplitude change was averaged for each month and plotted for a full year (Figure 4.8 (a)). The results are given by Figure 4.8 (b). Like Kikuchi (1986) it appears that there is no definite pattern in the data. The yearly mean value is about 7.3 dB and there is not a big variation around this value.

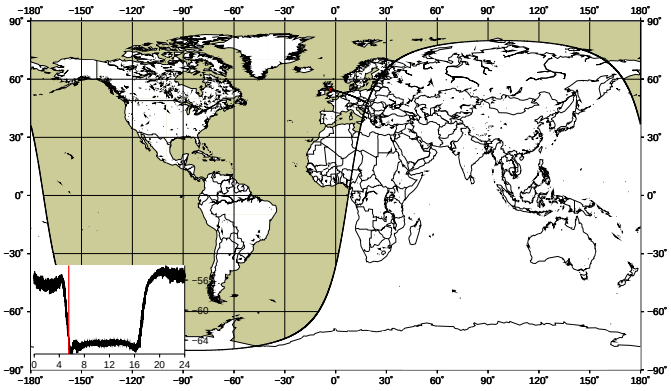

(a)

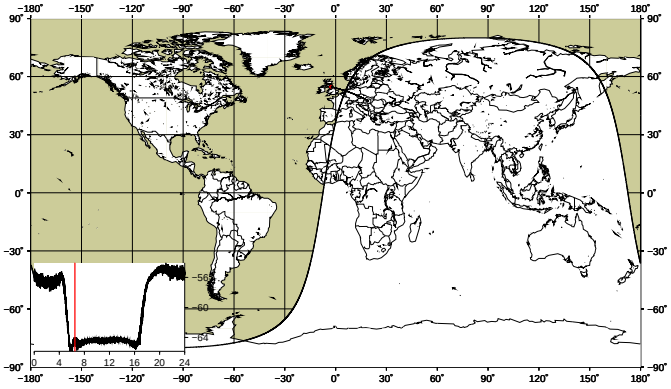

(b)

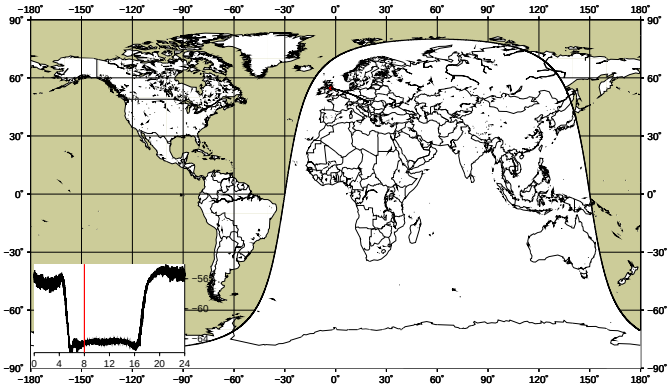

(c)

Figure 4.5: Frames from an animation illustrating the terminator effect where the transmitter is GBZ (refer to Table 4.1) and the receiver is located in Budapest, Hungary. (a) Sunrise occurring at the receiver. (b) Terminator lying between transmitter and receiver. Interference taking place between different modes modifying the amplitude profile. (c) Corresponding amplitude profile after terminator has crossed both the receiver and transmitter.

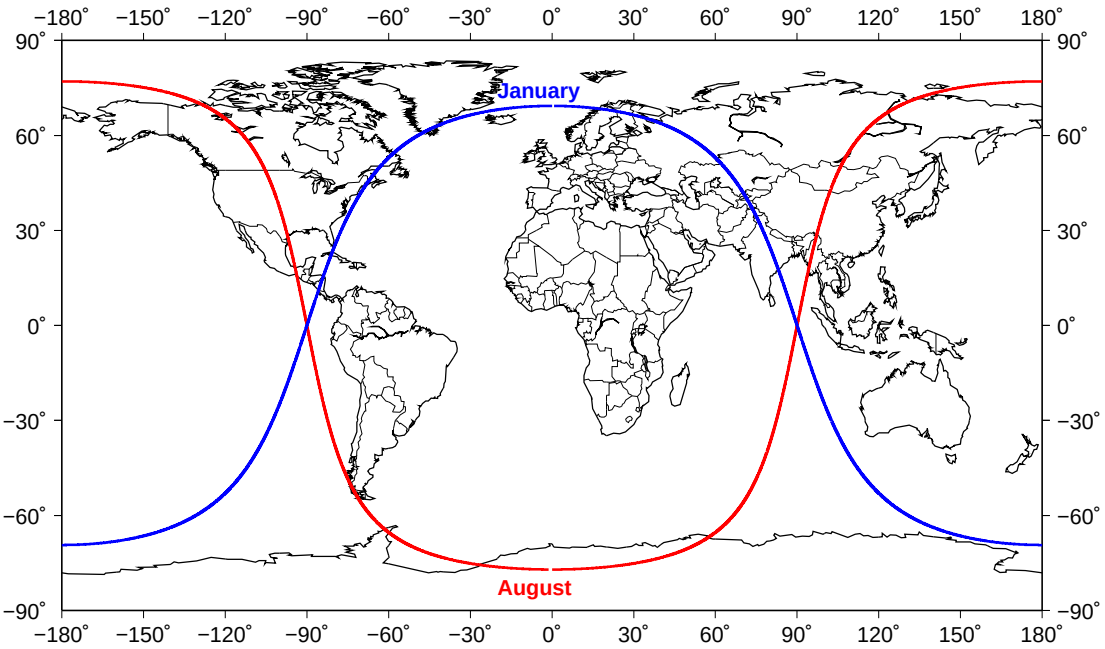

Figure 4.6: Terminator profile for 15 January and 15 August. The Sun is displayed for 12:00 UT for both of the days.

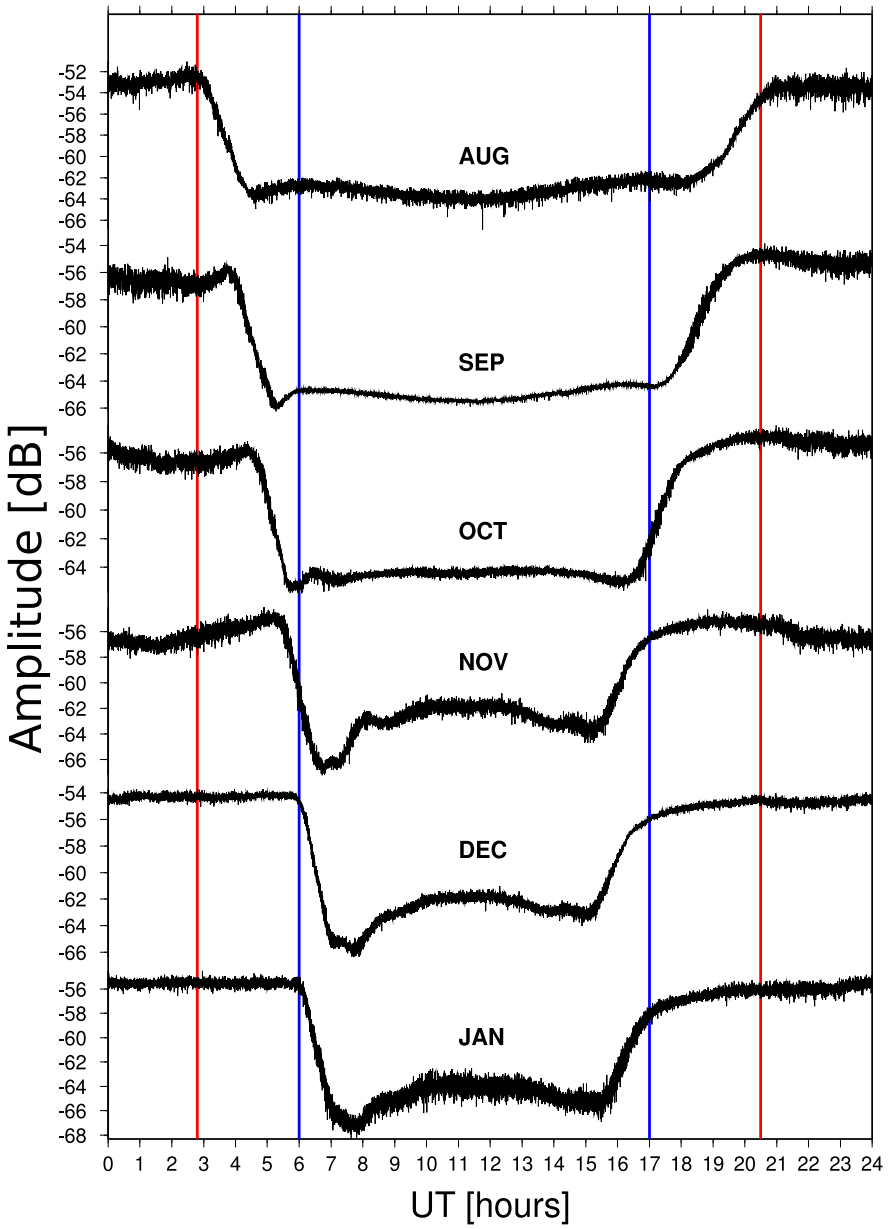

Figure 4.7: Monthly average for quite day variation on the GBZ ($19.6\,\mathrm{kHz}$) to Budapest path starting with August, 2007 (top) towards January, 2008 (bottom). The vertical lines on the outside represent when sunrise occur at summer and the vertical lines on the inside for winter.

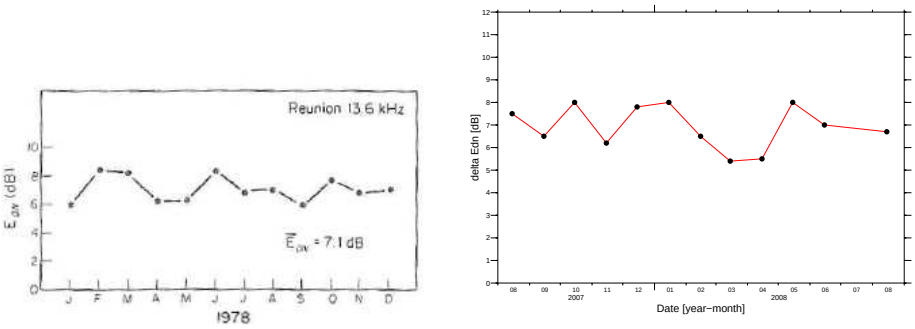

(a) (b)

Figure 4.8: (a) Monthly mean values of the diurnal amplitude change (E_{DN}) (Kikuchi, 1986). (b) The monthly averaged diurnal amplitude change taken from August 2007 - August 2008 at Tihany for the 19.6 kHz transmitter.

Chapter 5

Results

5.1 Summary of selected flares

From the available VLF data only transmitter paths which had continuous data for the day of flare were considered for detecting solar flare events. Generally the amplitude of the signal was considered with the exception of a few events where the phase was consistent for the days before and after a solar flare. The X-ray flux data was taken from the GOES-10 and GOES-11 satellites which both observed in the 0.05–0.4 nm and 0.1–0.8 nm bands. The sampling period for the search of solar flares based on the VLF data available was from 14 July 2007 to 17 May 2008.

The total number of flares detected by GOES for this period was 223. This included flares with X-ray fluxes less than 1.0 $\mu W/m^2$ (class C1.0 type flares). From this number only 5 events could be detected with either the amplitude or the phase of the VLF data. Like Grubor et al. (2008), only solar flares greater than class C1 are considered to be detectable. That in effect would have reduced the number of 223 events to 21 to be expected to be seen in the VLF data. It would also be sensible only to include those events which occurred in the "dayside" of the transmitter paths. This left 14 events for the sampling period of to be detected in at least one of the transmitter paths' VLF data.

Surprisingly this gave a "hit percentage" of 35.7% which is consistent with the results of Bain and Hammond (1975) (having a percentage of 35%) where the assumptions were quite similar regarding the magnitude of the class of the solar flares expected to be detected as well as the part of profile considered for looking at events.

5.2 Propagation paths

As described previously, H' and β plays a crucial role in describing the waveguide. Variation in the signal over a VLF path is seen as the solar zenith angle changes during the day. This affects the ionisation processes that takes place in the D-region leading to changes in β, which is mainly responsible for the variation in amplitude as the attenuation rates are changed, and changes in H' which causes changes in the relative phases and excitations of the modes.

Propagation over a long path can be expected to be more sensitive to β rather than H' because of its effect on the attenuation rate of the modes. While a longer path is more sensitive to β, a path that is too long will have a great variation in solar zenith angle, making it difficult to measure β. As described by Thomson (1993), for best results the Sun should be overhead near the centre of the path because the greatest range of the solar zenith angle will be measured as the day progresses.

A north-south path is also preferred since the solar zenith angle will reach a more clear cut minimum for most of the path at midday than for west-east paths. The paths that were used for monitoring the flares were all west-east paths because only data for these T_x/R_x configurations were available. The three receivers that were used are situated in Budapest, Tihany and Gyergyo. The propagation paths for Tihany can be seen in Figure 5.1. The receivers in Budapest and Gyergyo are situated slightly east of Tihany in that order. The transmitter ID's with their corresponding frequencies are given in Table 4.1.

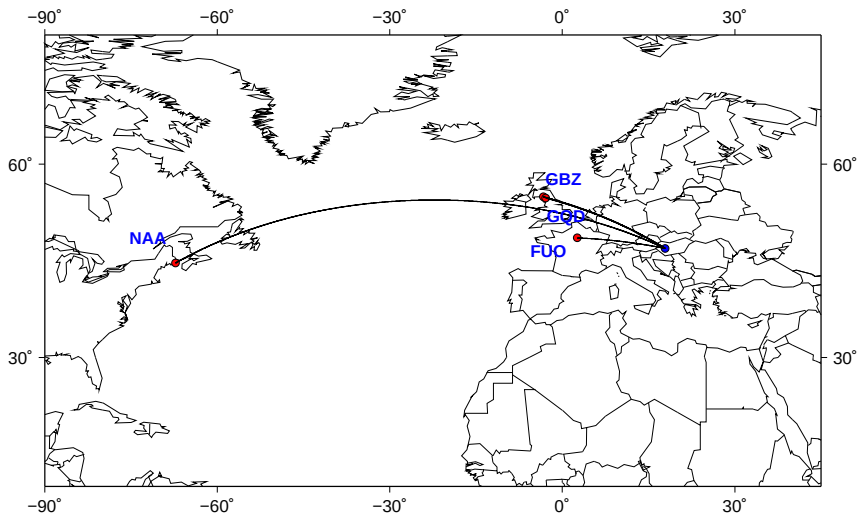

Figure 5.1: VLF transmitter paths for Tihany.

5.3 Flares detected by GOES evident in VLF data

The measured GOES X-ray fluxes are provided by the Space Physics Interactive Data Resource (SPIDR) (`http://spidr.ngdc.noaa.gov/spidr/index.jsp`). Depending on availability either GOES-10 or GOES-11 data were used. The sampling period of the VLF data recorded at the various stations is 0.05 seconds and was reduced to 5 seconds after a "box-car" average was applied to the data. A summary of the flares that were detected by the GOES satellites that also appeared in the VLF data can be seen in Table 5.1. Table 5.2 gives a summary of where the different flares were recorded for a corresponding transmitting frequency. Each event is also briefly described in the subsections to follow.

Table 5.1: Summary of all the selected flaresdetected by the GOES satellites and Solar Monitor. The time at which the peak of the flare was reached is given with its class, X-ray flux magnitude, flare number given by Solar Monitor and flare number given by GOES.

Date	Peak Time [UT]	Class	Satellites	Flux [$\mu W/m^2$]	SM Number	GOES Number
06/08/2007	09:13	C1.5	GOES-11	1.5	10966	5690
24/08/2007	07:54	C2.0	GOES-10	2.0	10969	6000
13/12/2007	10:03	C4.5	GOES-10 GOES-11	4.5	10978	7660
14/12/2007	14:16	C1.1	GOES-10	1.1	10978	7820
18/12/2007	13:20	C2.1	GOES-11	2.1	10978	8230

Table 5.2: Summary of flares recorded at different stations (Budapest, Tihany and Gyergyo) in either amplitude or phase.

Date	19.6 kHz	20.9 kHz	22.1 kHz	24.0 kHz
06/08/2007	Thy (amp)	-	-	-
24/08/2007	Bud (amp) Thy (amp)	-	-	-
13/12/2007	Bud (amp) Gye (amp) Thy (amp)	Bud (amp) Gye (amp)	Bud (phase)	-
14/12/2007	Gye (amp)	-	-	Bud(amp)
18/12/2007	Thy (amp)	Gye (amp)	Bud (phase)	-

GOES defines the start of a flare to be the time at which there is a sudden increase from the daily X-ray flux profile. By the GOES classification method a flare is only considered to have ended once the flux has dropped under the half-way mark of the peak flux, this would also define the duration of the flare when referring to the X-ray flux. When referring to the flare in the VLF data it might be that the start of the flare given by GOES might be slightly earlier than the onset of the flare in the VLF data. The duration of the flare in the VLF data will be defined as from the onset up to the time where the signal returns

to the diurnal profile if compared to the monthly averaged diurnal profile.

5.3.1 Flare of 6 August 2007

On 6 August 2007 there were 3 flares which started at 09:05, 15:24 and 22:40 UT. The flare of interest started at 09:05, ended at 09:21 and had a peak at 09:13 UT (GOES classification) with a flux of 1.5 $\mu W/m^2$ (Figure 5.2). The flare is listed as a class C1.5 flare by GOES. The flare was detected at Tihany in the amplitude of the 19.6 kHz signal. Only the first few hours of that specific day's data were available. From Figure 5.3 it is seen that the amplitude profile kept reasonable constant during the day up to the flare. About 09:07 the flare caused a decrease in the amplitude of the signal. The flare had its maximum effect in the amplitude 6 minutes after the onset. The duration of the flare after was 12 minutes.

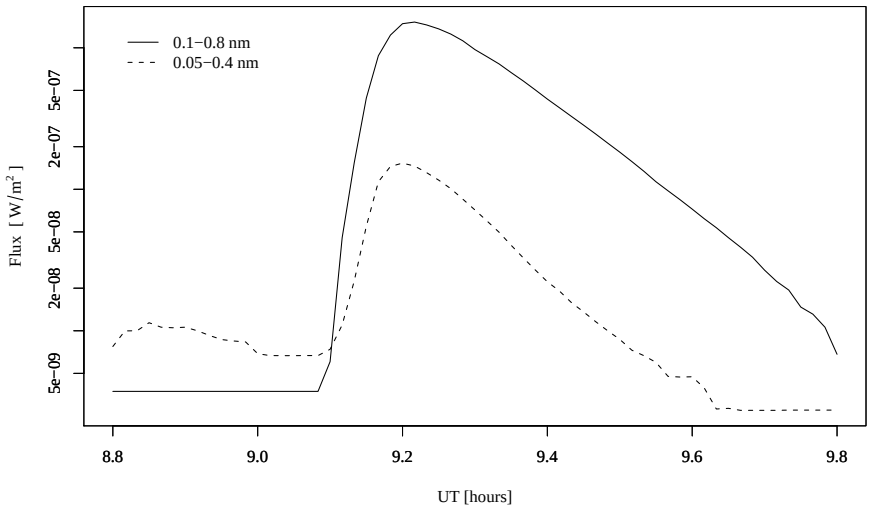

Figure 5.2: GOES-11 X-ray flux data for 06 August 2007 in the 0.05–0.4 nm and 0.1–0.8 nm bands.

5.3.2 Flare of 24 August 2007

Four flares occurred on 24 August 2007, 3 of which were below class C1 and the flare of interest has a class of C2.0. The flare started at 07:49, ended at 07:58 and had a peak at 07:54 (GOES classification) of 2.0 $\mu W/m^2$ detected by GOES-10 (Figure 5.4). The flare was detected in the amplitude data at Tihany and Budapest for the 19.6 kHz transmitter. The diurnal amplitude profiles for Budapest and Tihany look similar. Referring to Figures

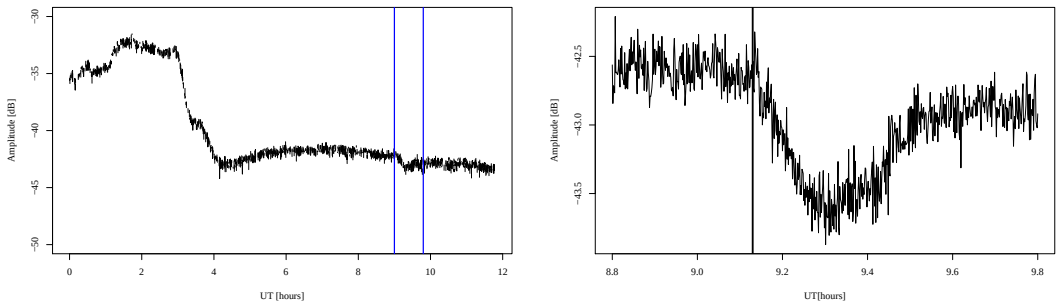

Figure 5.3: Amplitude of 19.6 kHz signal recorded at Tihany on 6 August 2007.

5.5 and 5.6, the onset of the flare occurred at 07:52 when the amplitude started to decrease and reached a minimum at 07:55. The duration of the flare in the flux (Figure 5.4) is about 24 minutes and with some uncertainty (because of the noise) it seems to be similar in the VLF data (Figures 5.5 and 5.6).

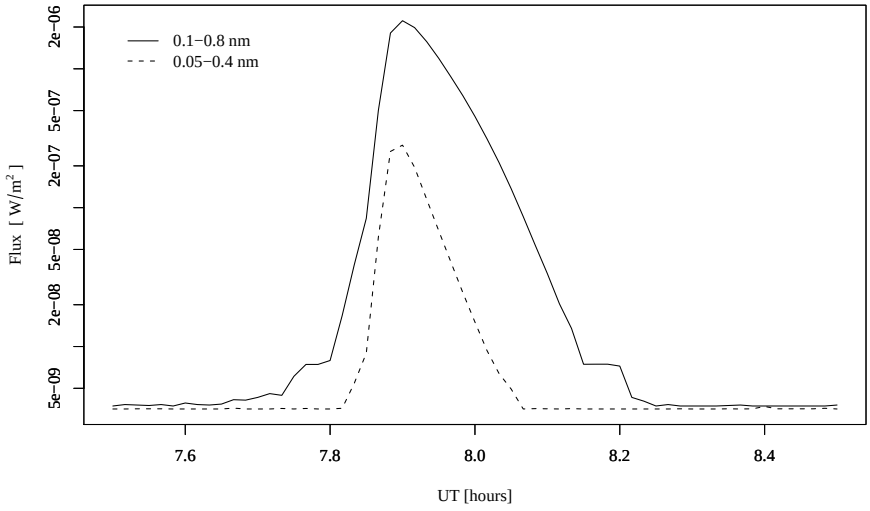

Figure 5.4: GOES-10 X-ray flux data for 24 August 2007 in the 0.05–0.4 nm and 0.1–0.8 nm bands.

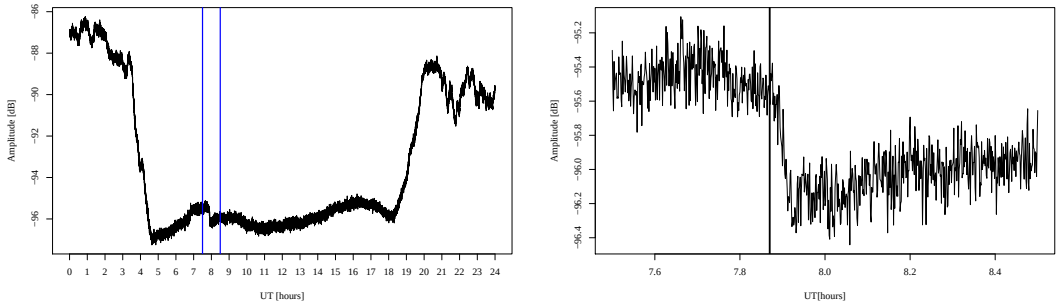

Figure 5.5: Amplitude of 19.6 kHz signal recorded at Tihany on 24 August 2007.

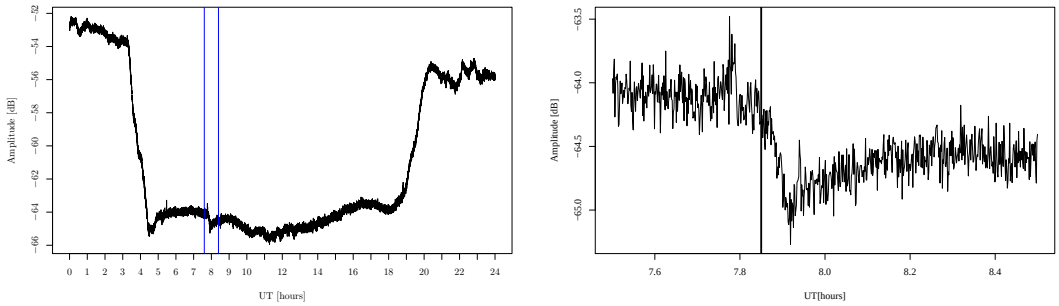

Figure 5.6: Amplitude of 19.6 kHz signal recorded at Budapest on 24 August 2007.

5.3.3 Flare of 13 December 2007

13 December 2007 was a very eventful day, having 21 flares detected by the GOES-10 and GOES-11 satellites. From these events, 18 were below the C1 class. One flare was not considered since it occurred during the night over all the transmitter paths. The flare of interest is showed in Figure 5.7. The flare, which is of class C4.5, started at 09:39, ended at 10:09 and had a peak at 10:03 (GOES classification) with a flux of 4.5 $\mu W/m^2$. The flare was detected on 3 transmitter frequencies. For the 19.6 kHz transmitter a decrease in amplitude was found at the Tihany (Figure 5.8) and Budapest (Figure 5.9) and an increase at Gyergyo (Figure 5.10). For the 20.9 kHz transmitter an increase in amplitude was found at Budapest (Figure 5.11) and a decrease at Gyergyo (Figure 5.12). For the 22.1 kHz transmitter there was an increase in the phase at the Budapest (Figure 5.13) receiver. The flare itself is very interesting because there are two X-ray flux peaks. This is not unusual for a flare. Since the flux did not drop to half of the flux after the first peak, this first peak is part of the event.

There was also one flare that started at 13:59 and ended at 14:06 that does not seem to appear in the VLF signals.

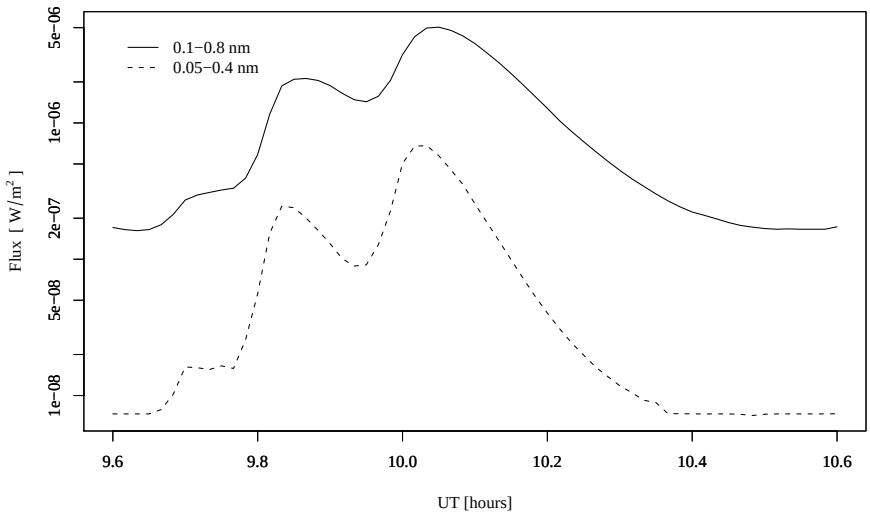

Figure 5.7: GOES-10 X-ray flux data for 13 December 2007 in the 0.05–0.4 nm and 0.1–0.8 nm bands.

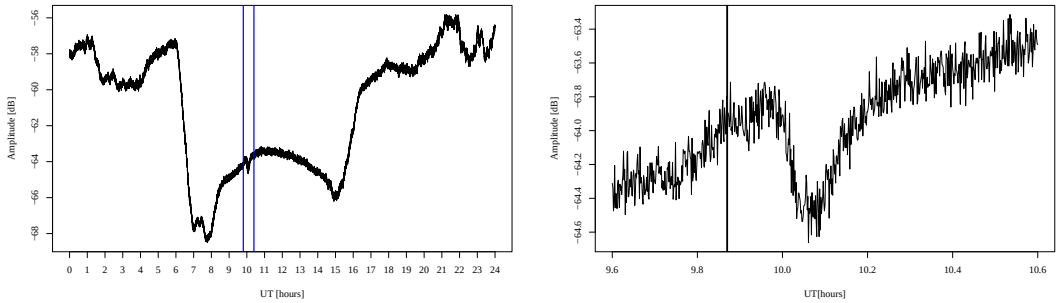

Figure 5.8: Amplitude of 19.6 kHz signal recorded at Tihany on 13 December 2007.

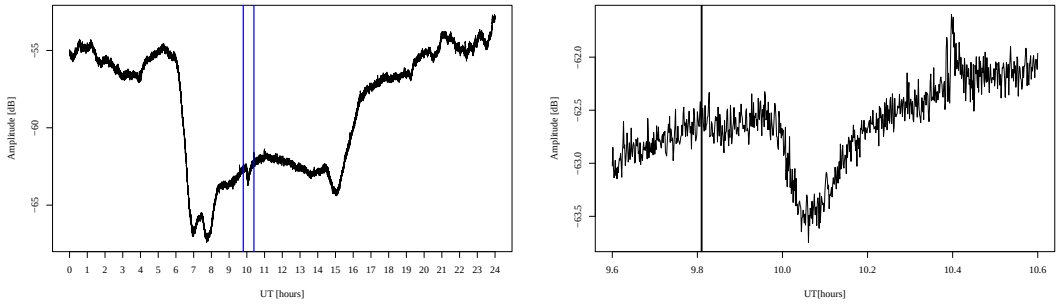

Figure 5.9: Amplitude of 19.6 kHz signal recorded at Budapest on 13 December 2007.

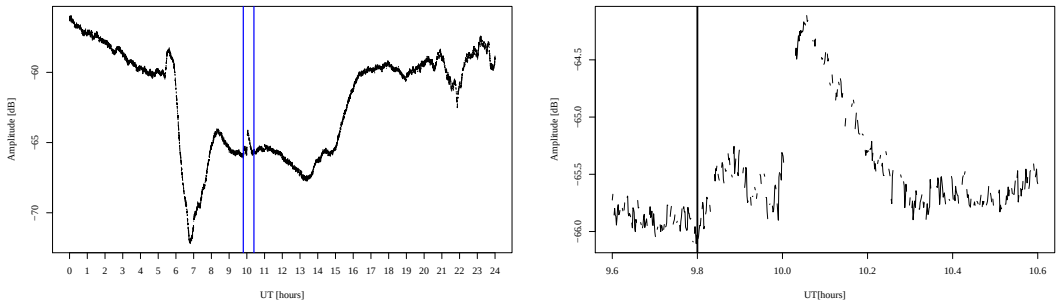

Figure 5.10: Amplitude of 19.6 kHz signal recorded at Gyergyo on 13 December 2007.

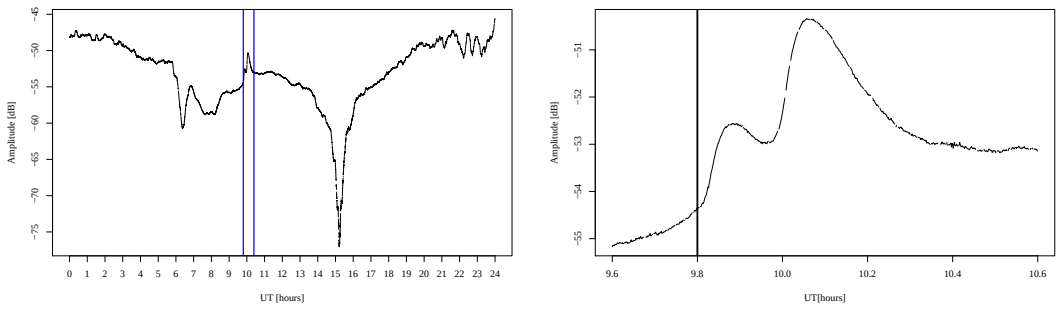

Figure 5.11: Amplitude of 20.9 kHz signal recorded at Budapest on 13 December 2007.

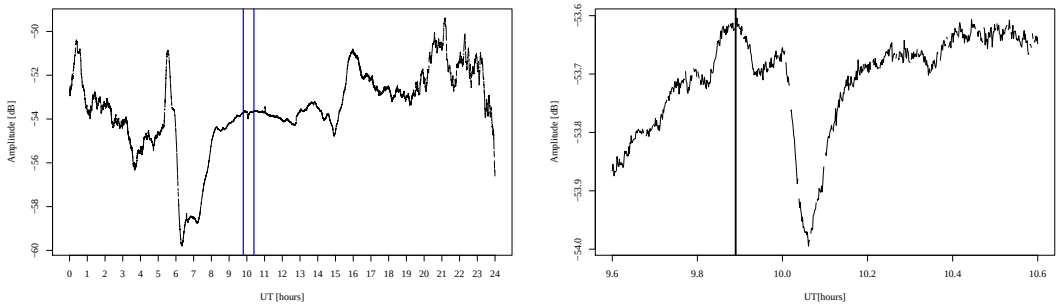

Figure 5.12: Amplitude of 20.9 kHz signal recorded at Gyergyo on 13 December 2007.

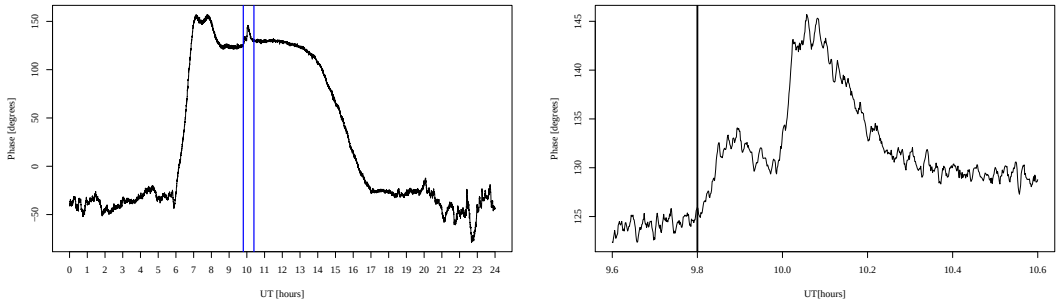

Figure 5.13: Phase of 22.1 kHz signal recorded at Budapest on 13 December 2007.

5.3.4 Flare of 14 December 2007

From the 9 flares occurring on 14 December 2007, 7 were weaker than class C1. A flare of class C1.1 starting at 08:13 did not feature in any of the VLF data. The flare that did feature in the VLF data started at 14:11, ended at 14:21 and had a peak of 1.1 $\mu W/m^2$ at 14:16 (GOES classification) that was detected by the GOES-10 satellite, see Figure 5.14. From the Gyergyo receiver a decrease in amplitude can be seen for the 19.6 kHz transmitter (Figure 5.15). An increase in amplitude can be seen at Budapest receiver for the 24.0 kHz transmitter (Figure 5.15). The onset of the flare occurred at 14:13 on both the receivers where the peak of the flare showed 2 minutes later in the data. The duration of the flare was about 11 minutes after which the amplitude recovered.

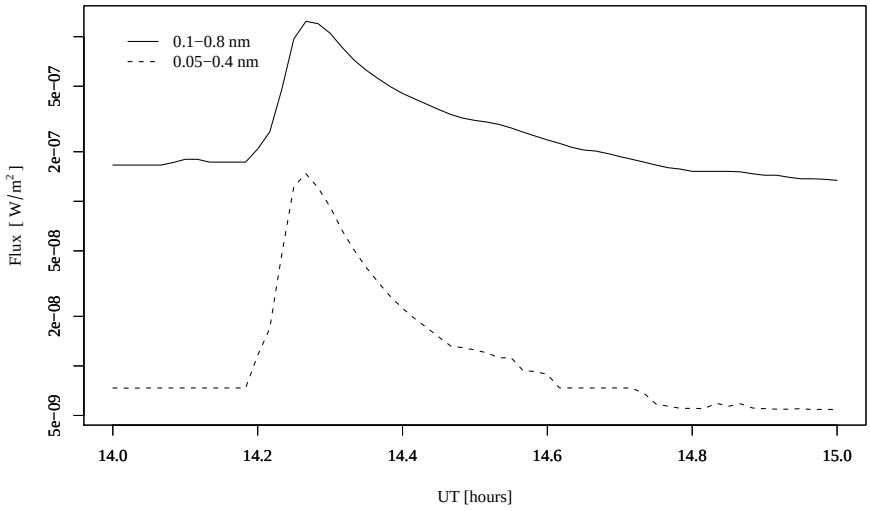

Figure 5.14: GOES-10 X-ray flux data for 14 December 2007 in the 0.05–0.4 nm and 0.1–0.8 nm bands.

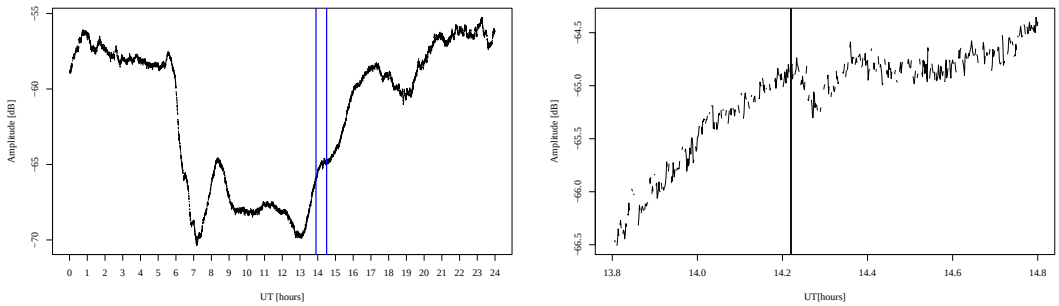

Figure 5.15: Amplitude of 19.6 kHz signal recorded at Gyergyo on 14 December 2007.

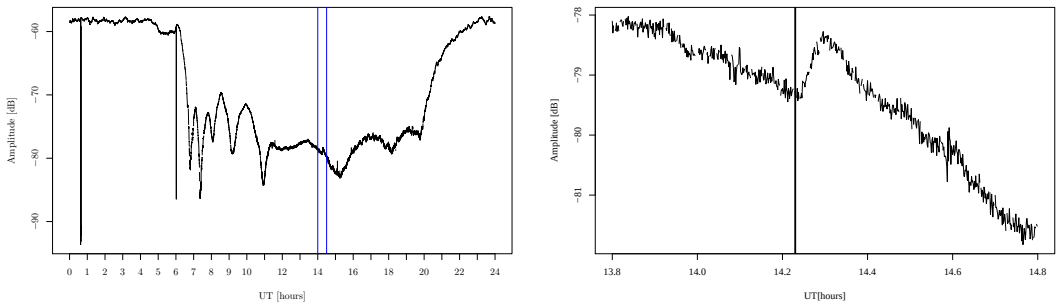

Figure 5.16: Amplitude of 24.0 kHz signal recorded at Budapest on 14 December 2007.

5.3.5 Flare of 18 December 2007

The last identified flare occurred on 18 December 2007, an extremely eventful day, similar to the one on 13 December 2007. During the day 22 flares occurred, of which 19 were below class C1.0. The flare that was detected in the VLF data started at 13:08, ended at 13:29 and had a peak of 2.1 $\mu W/m^2$ at 13:20 (GOES classification) and was detected by GOES-11, see Figure 5.17. An increase in amplitude can be seen at Tihany receiver for the 19.6 kHz transmitter (Figure 5.18). From the Gyergyo receiver a decrease in amplitude can be seen for the 20.9 kHz transmitter (Figure 5.19). This is the only other identified flare that was detected in the phase of the signal. It was recorded at Budapest for the 22.1 kHz transmitter with an advance in the phase of the signal (Figure 5.20). The event will be studied in more detail in the section to follow.

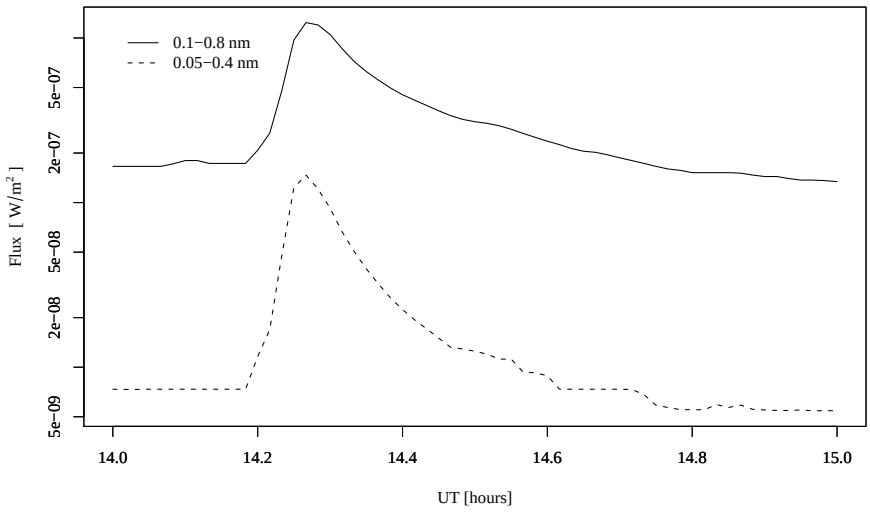

Figure 5.17: GOES-11 X-ray flux data for 18 December 2007 in the 0.05–0.4 nm and 0.1–0.8 nm bands.

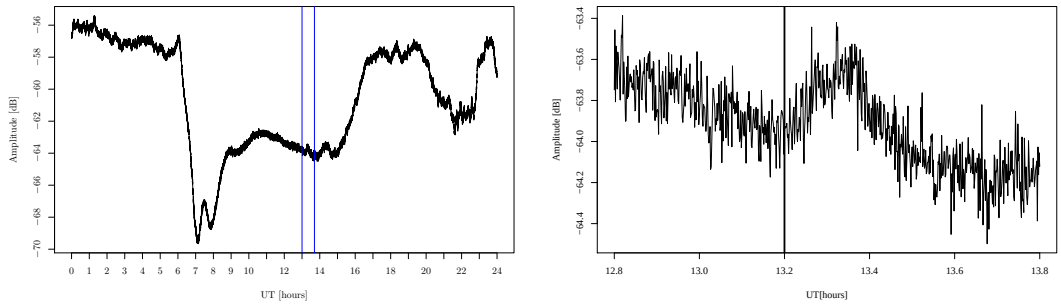

Figure 5.18: Amplitude of $19.6\ \mathrm{kHz}$ signal recorded at Tihany on 18 December 2007.

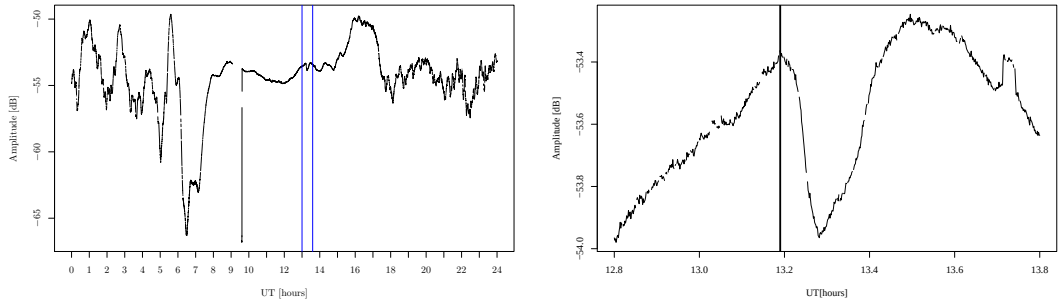

Figure 5.19: Amplitude of $20.9\ \mathrm{kHz}$ signal recorded at Gyergyo on 18 December 2007.

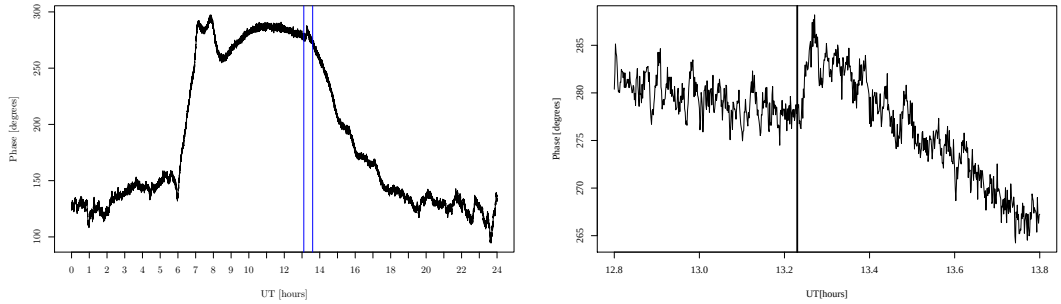

Figure 5.20: Amplitude of $22.1\ \mathrm{kHz}$ signal recorded at Gyergyo on 18 December 2007.

5.4 Case study: 13 December 2007

Although 5 different events were detected only two are studied in depth. The first event of interest is the one that occurred on 13 December 2007. Specifically, this event is chosen because it has the greatest magnitude and was detected on several propagation paths. It was also close to the middle of the amplitude and phase versus time profile on the dayside when the event occurred.

The event was observed on 6 different propagation paths and at 3 different frequencies. The solar flare was imaged in several wavelength bands and is provided by the Solar Monitor at `http://www.solarmonitor.org` (see Figure 5.21). There is clear evidence of the flare in both the extreme ultraviolet images and magnetograms. The eruption is seen near the centre of the Sun in the bottom right quadrant.

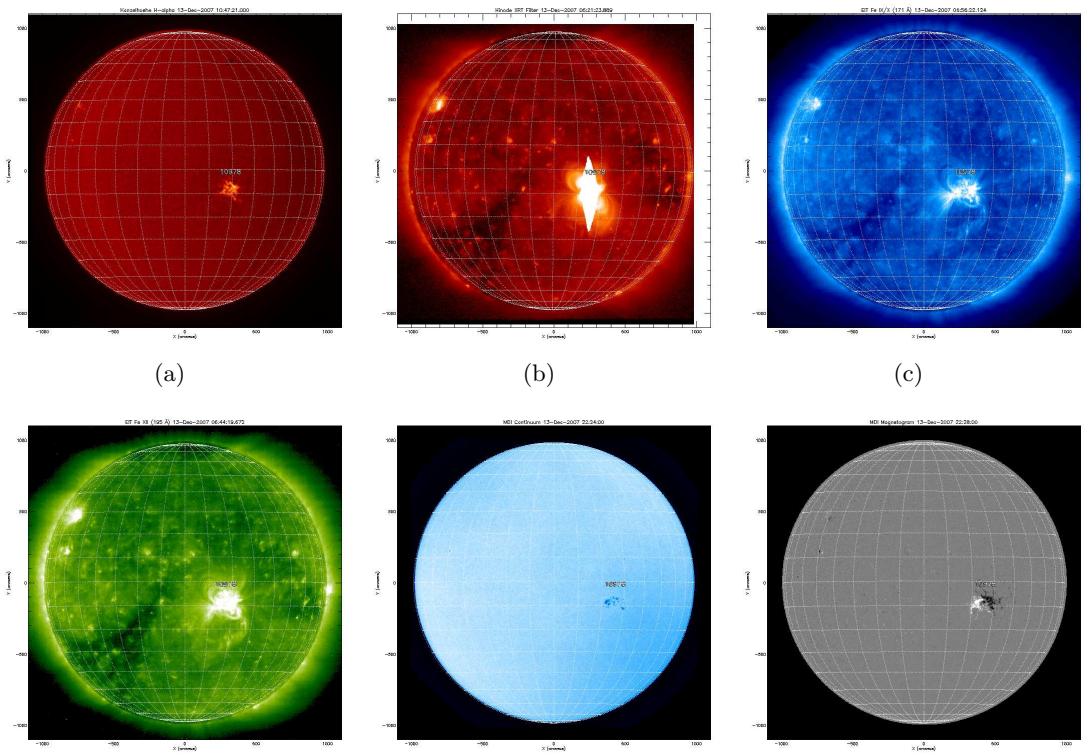

(a) (b) (c)

(d) (e) (f)

Figure 5.21: Images taken of the Sun during the solar flare on 13 December 2007 (http://www.solarmonitor.org). (a) Global H-α Network image, showing the Sun in the H-α emission line at 10:47 UT. (b) Hinode/XRT image of the corona in x-ray at 06:21 UT. (c) Extreme Ultraviolet Imaging Telescope, the corona in EUV light, in the 17.1 nm band at 06:56 UT. (d) Extreme Ultraviolet Imaging Telescope, the corona in EUV light, in the 19.5 nm band at 06:44 UT. (e) Michelson Doppler Interferometer (MDI) continuum image, showing the photosphere in white light at 22:24 UT. (f) MDI magnetogram showing the line-of-sight magnetic field in the photosphere at 22:28 UT. The solar flare is seen quite close to the centre of the Sun in the bottom right quadrant.

5.4.1 Extracting H' and β

The way LWPC was used was to rather find a reasonable constant change in amplitude and phase that LWPC outputs that compares well with the observations. For example it was found that when values for $H' = 75$ km and $\beta = 0.32\,\mathrm{km}^{-1}$ were chosen for the unperturbed midday conditions that there was a consistency over all the propagation paths for the change in H' and β. From Table 5.3 the average for the reference height at the peak X-ray output of the flare is $H' = 70.8$ km. For the sharpness parameter it is $\beta = 0.39\,\mathrm{km}^{-1}$.

Table 5.3: Calculated β and H' values from LWPC for propagation paths for 13 December 2007. $\triangle$A and $\triangle$P are the changes in VLF amplitude and phase.

Frequency (kHz)	Receiver	GCP (distance)	$\triangle$A (dB)	$\triangle$P (deg)	β (km^{-1})	H' (km)
19.6	Budapest	1720	1.1	-	0.39	72.0
19.6	Tihany	1687	0.78	-	0.39	72.0
19.6	Gyergyo	2174	1.72 (inc)	-	0.40	72.3
20.9	Budapest	1602	3.8 (inc)	-	0.41	65.5
20.9	Gyergyo	2058	0.36	-	0.38	71.7
22.1	Budapest	1540	-	18.3	0.37	71.4

Consider the values calculated for the 19.6 kHz signal from Table 5.3. All the computed values of H' and β at the different receivers compare well with one another even when there was an increase measured in the amplitude at Gyergyo.

For the 20.9 kHz signal different values were found at the receivers. The values of β and H' at Gyergyo are quite similar to those of the 19.6 kHz signal paths. For the 20.9 kHz signal recorded at Budapest the change in amplitude was found to be more sensitive to H'. With such a high increase in amplitude observed at the receiver, for LWPC to match the amplitude, it calculates H' to be much lower than what was calculated at other receivers.

For the 22.1 kHz signal at Budapest, the phase advanced with 18.3 degrees as the reflection height was lowered for this period (Figure 5.13). Both the calculated values for β and H' are less than those for the 19.6 kHz signal paths.

Neglecting the calculated values for H' and β using LWPC for the 20.9 kHz–Budapest path and taking the average values for H' and β on all of the other paths one has $H' = 71.8$ km and $\beta = 0.39\,\mathrm{km}^{-1}$. These values for H' and β are used in the following sections to construct the electron density profile and modal interference figures. From the unperturbed conditions ($H' = 75$ km and $\beta = 0.32\,\mathrm{km}^{-1}$), the flare caused H' to

decrease to a height of 71.8 km, giving a total change of 3.1 km during the peak time of the flare. β was increased to 0.39 km^{-1} at the peak time of the flare, giving a total change of 0.07 km^{-1}.

5.4.2 Electron density profile and modal interference

Using (1.2) the electron density profile can be constructed using the calculated values for H'=71.8 km and $\beta = 0.39\ km^{-1}$. Both the electron density versus height profile for the unperturbed quiet day and for the perturbed solar flare event are constructed and shown in Figure 5.22.

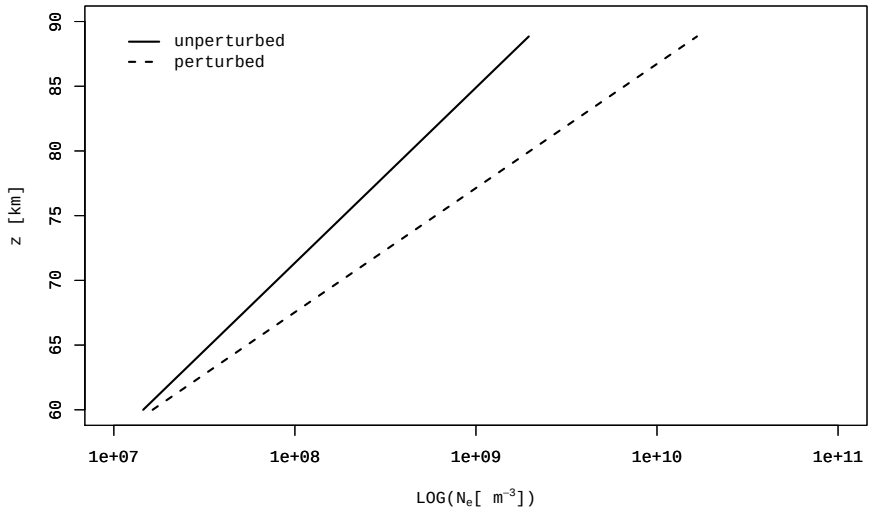

Figure 5.22: Electron density profile on 13 December 2007 for the quiet unperturbed and perturbed ionosphere at the peak of the flare, 10:06 UT.

During the solar flare the slope of the electron density profile is increased as β increased from the unperturbed quiet day profile. The extra X-rays that are provided by the flare ionised the D-region further into lower regions resulting in an increase of electrons in those lower regions explaining why there is an increase in the slope of the electron density profile. This increase in electron density throughout z = 60–90 km is of great importance for VLF propagation, affecting the amplitude and phase of the signal.

LWPC also allows one to simulate the signal for Great Circle Path (GCP) distances measured from the transmitter. From the calculated values of $H' = 71.8$ km and $\beta = 0.39\ km^{-1}$ the amplitude variation versus distance is calculated for the 19.6 kHz and 20.9 kHz GCP (see Figures 5.23–5.24). The vertical solid lines inserted in each one of the figures represents the distance from the transmitter to the appropriate receivers.

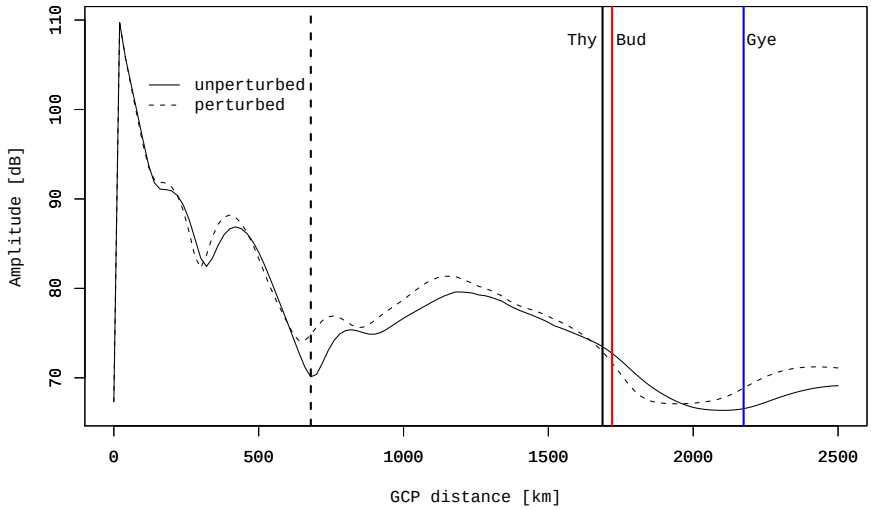

Figure 5.23: Calculated variation in amplitude of the 19.6 kHz signal as a function of distance along the GCP for 13 December 2007. The vertical dashed line represents an example of a modal minimum for unperturbed conditions.

First consider Figure 5.23 for the 19.6 kHz signal. The change in amplitude at the different receivers compares well with the observed values given Table in 5.3. It can be seen that there was a decrease in amplitude at Budapest and Tihany and an increase at Gyergyo. An example of an interference minimum on the unperturbed quiet day is seen at 680 km from the transmitter. This location of the minimum on the GCP would be more sensitive to VLF-monitoring. During the solar flare all the modal minima are found to move towards the transmitter as with the findings of Thomson and Clilverd (2001).

Figure 5.24 for 20.9 kHz shows a small increase in amplitude at Budapest and a small decrease at Gyergyo. Even with only a reference height of $H' = 71.8$ km an increase at the Budapest receiver can be seen. The simulation favours Gyergyo since its computed values for H' and β are much closer than those for Budapest. A modal interference minimum occurred at 760 km from the transmitter for unperturbed conditions and during the flare it moved towards the transmitter.

For the 22.1 kHz signal only the phase data at Budapest was used since the amplitude data was bad. The simulation shows the phase advance at the receiver that is also observed (Table 5.3). One of the interference modal minima moved from 1000 to 920 km towards the transmitter at the peak time of the flare (Figure 5.25).

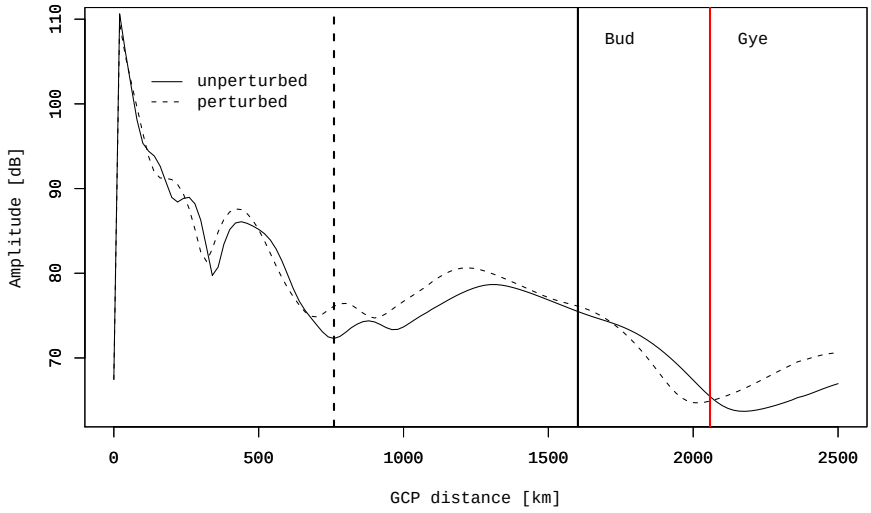

Figure 5.24: Calculated variation in amplitude of the $20.9\ \mathrm{kHz}$ signal as a function of distance along the GCP for 13 December 2007. The vertical dashed line represents an example of a modal minimum for unperturbed conditions.

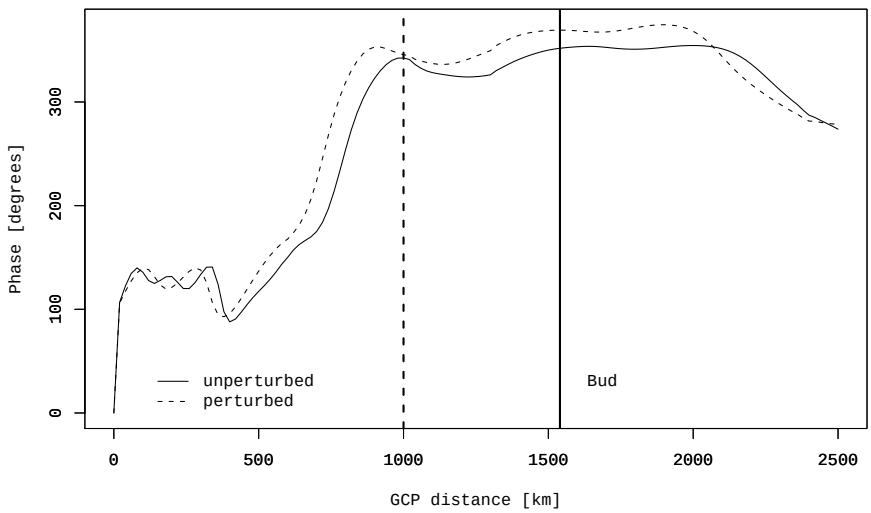

Figure 5.25: Calculated variation in phase of the $22.1\ \mathrm{kHz}$ signal as a function of distance along the GCP for 13 December 2007. The vertical dashed line represents an example of a modal minimum for unperturbed conditions.

5.4.3 Comparing flux data with VLF amplitude and phase data

One of the current problems with the satellite X-ray flux detectors is that when a solar flare of great magnitude occurs, it saturates the detectors, making it impossible to track the size of the flare and losing some information about the flare. Again looking at the event of 13 December 2007, the results are given and discussed in an attempt to show that the X-ray flux and VLF data are linearly related. This event, however, is by a great magnitude smaller than other events to which this technique has been applied. For example, this event has a flux of 4.5 $\mu W/m^2$ compared to events with fluxes of 1.0 mW/m^2 (Thomson et al., 2004).

Because there is a daily pattern in the VLF data incorporated as a result of the changing solar zenith angle, the average quiet day amplitude and phase profile were subtracted from the one on which the flare occurred. A fast discrete Fourier transform was applied to the data, transforming the data into the frequency domain. A low pass block filter was then used to set the high order harmonic components to zero and leave the low frequencies unaffected. An inverse Fourier transform was then applied to transform the data, with the unwanted frequencies removed, back to the time domain. This was done to smooth out the VLF data to compare it with the flux data. The sampling period of the VLF was $T = 5$ seconds. The Nyquist frequency is then $f_N = 0.1$ Hz. The result of the low pass filter was defined to remove components with periods shorter than 0.00249 Hz. The fits of the data at the different receivers are given by Figure 5.26

The signature in the D-region was expected to be appear quite soon after incidence of the X-rays into the atmosphere. Figures 5.27–5.31 show the comparison between VLF amplitude and the X-ray flux data. One can see that both the peaks in the flux data follow the VLF data. The 19.6 kHz/Gyergyo (Figure 5.30) and 20.9 kHz/Budapest (Figure 5.29) amplitude data show a linear relationship with the 0.1–0.8 nm band flux data while the rest of amplitude data does not compare that well. The amplitude in all the data except for 19.6 kHz/Gyergyo falls off more rapidly after the flare had reached its peak. When one looks at the phase (Figure 5.32), comparing it with the 0.05–0.4 nm band, it also seems quite late to react on the effect of the X-rays and recovers slowly from it. The phase compares well with the 0.1–0.8 nm band. The change in phase seems linearly proportional to the change in the flux. Especially just up to the peak, the phase tracks the flux very well. After the peak is reached the phase falls off from the flux data. The phase seems to be slow to recover from the flare.

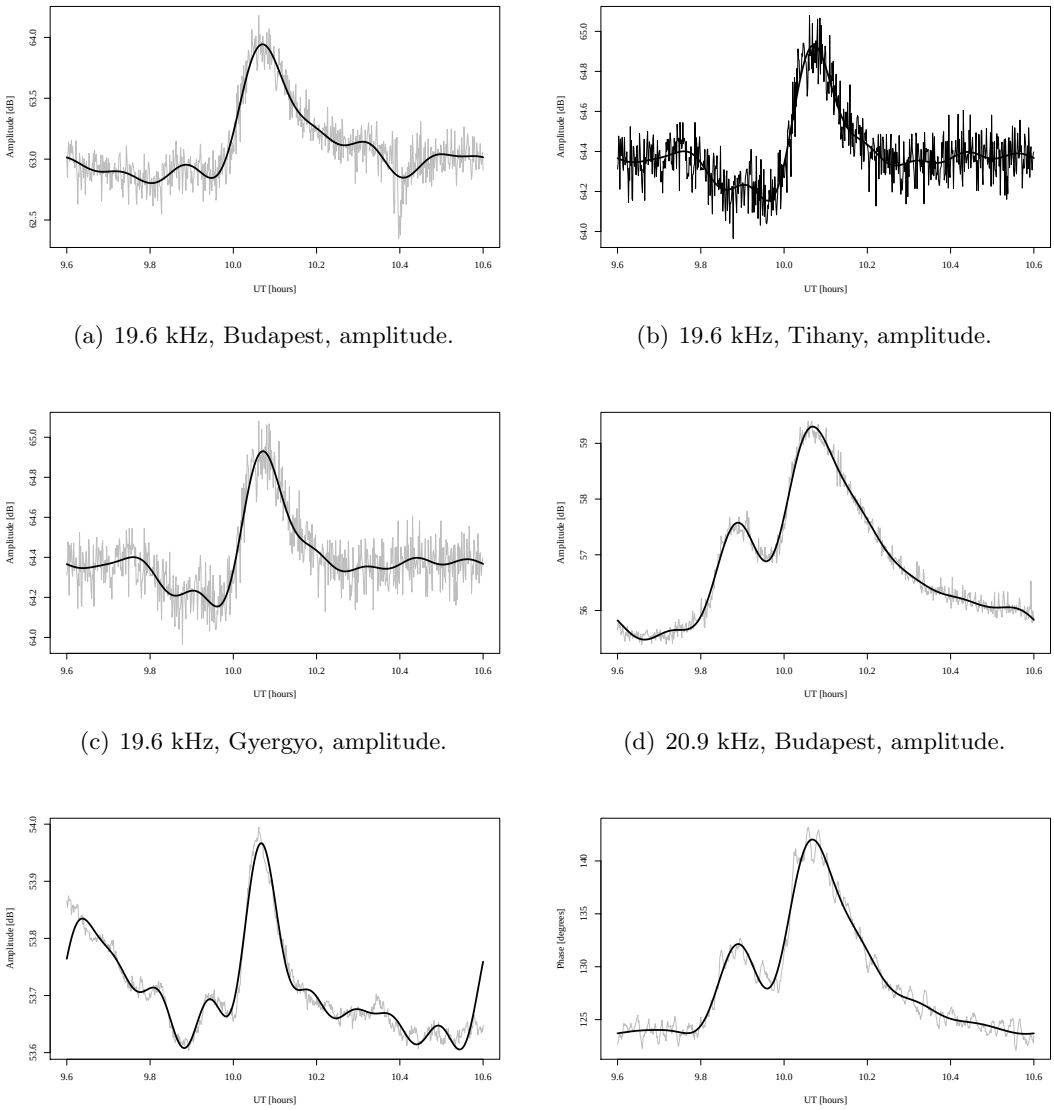

(a) 19.6 kHz, Budapest, amplitude.

(b) 19.6 kHz, Tihany, amplitude.

(c) 19.6 kHz, Gyergyo, amplitude.

(d) 20.9 kHz, Budapest, amplitude.

(e) 20.9 kHz, Gyergyo, amplitude.

(f) 22.1 kHz, Budapest, phase.

Figure 5.26: The fit for 13 December 2007 after a Fourier reconstruction was applied to the VLF data at the different receivers.

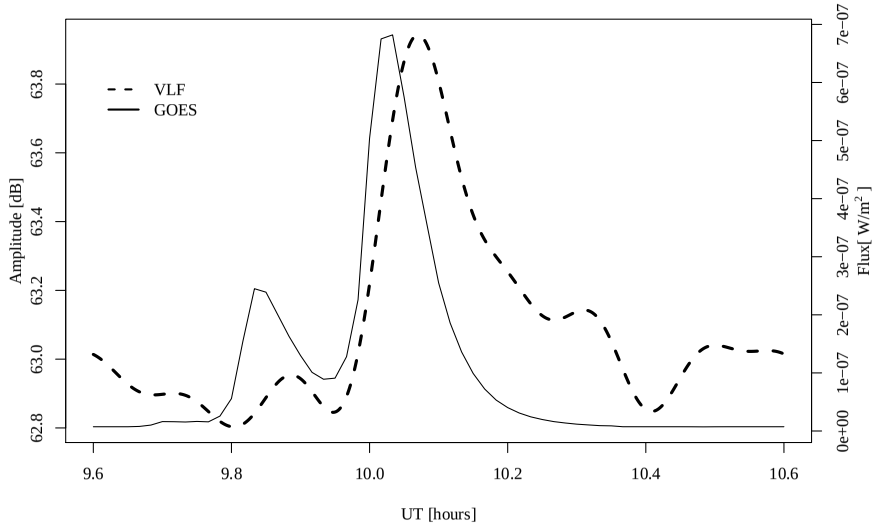

(a) 0.05–0.4 nm, 19.6 kHz Budapest.

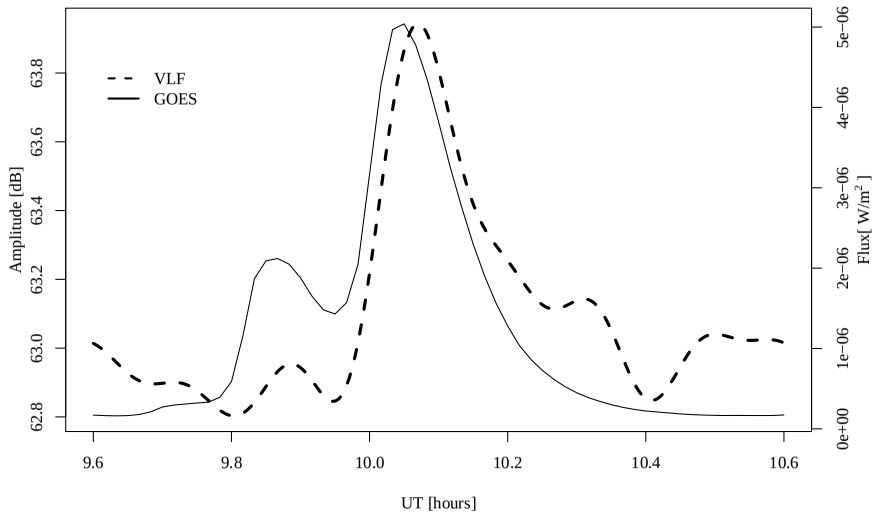

(b) 0.1–0.8 nm, 19.6 kHz Budapest.

Figure 5.27: Amplitude on 13 December 2007 of the 19.6 kHz signal at Budapest with GOES X-ray flux.

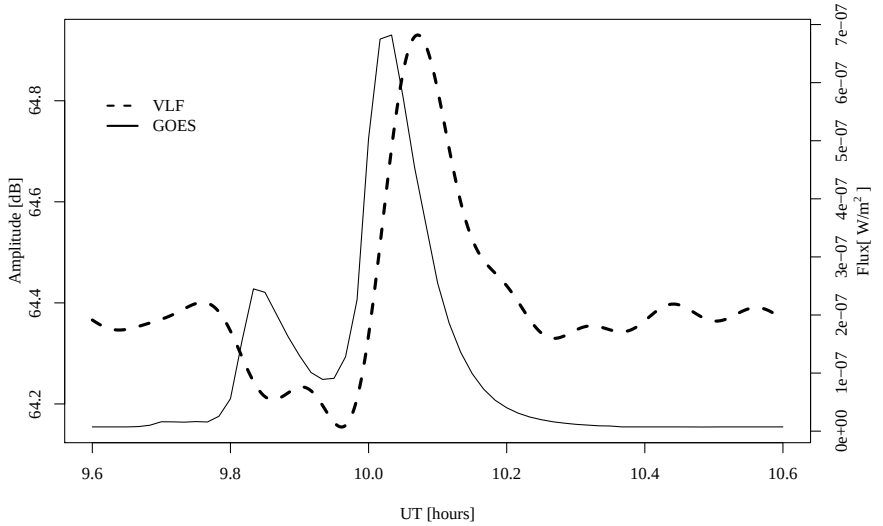

(a) 0.05–0.4 nm, 19.6 kHz Tihany.

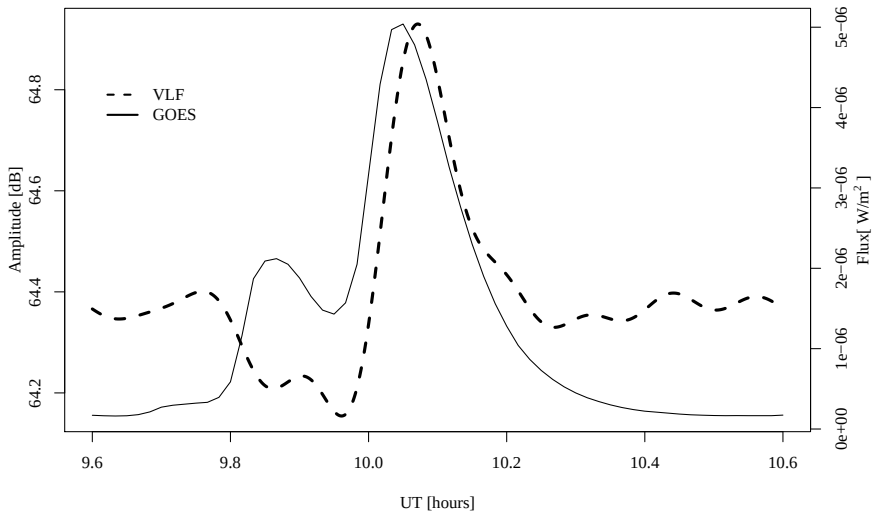

(b) 0.1–0.8 nm, 19.6 kHz Tihany.

Figure 5.28: Amplitude on 13 December 2007 of the 19.6 kHz signal at Tihany with GOES X-ray flux.

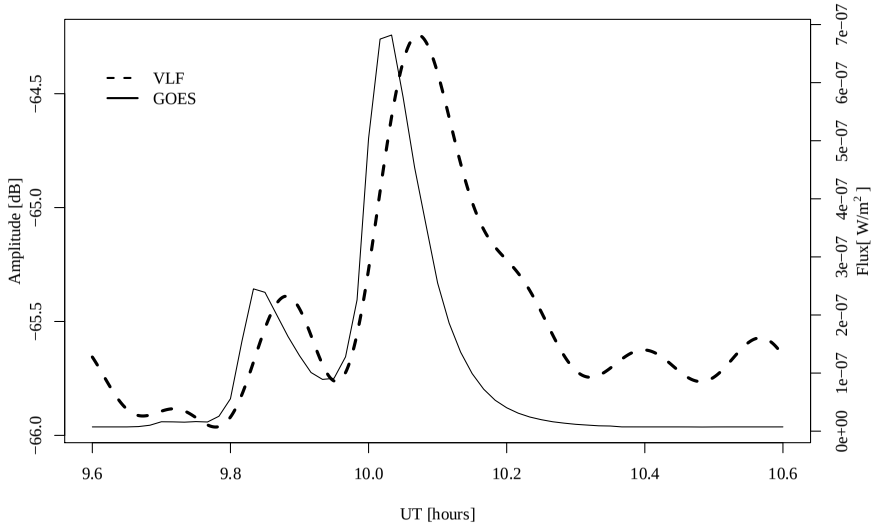

(a) 0.05–0.4 nm, 19.6 kHz Gyergyo.

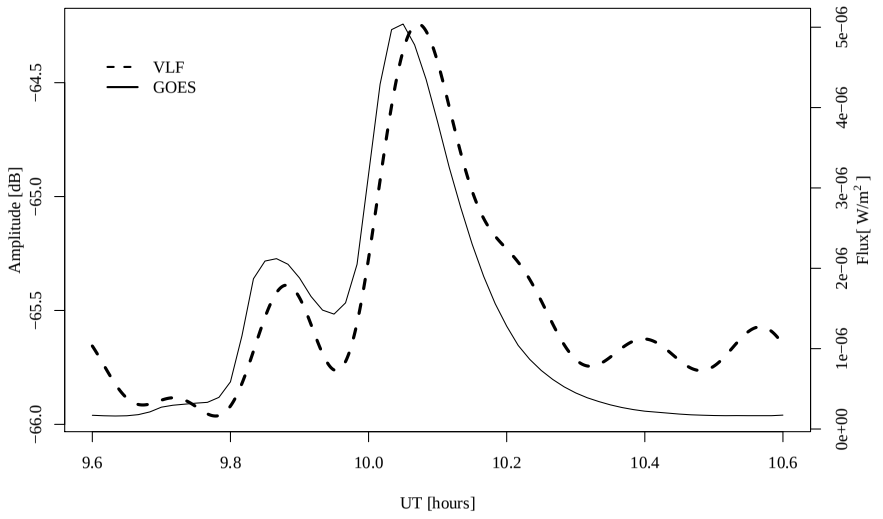

(b) 0.1–0.8 nm, 19.6 kHz Gyergyo.

Figure 5.29: Amplitude on 13 December 2007 of the 19.6 kHz signal at Gyergyo with GOES X-ray flux.

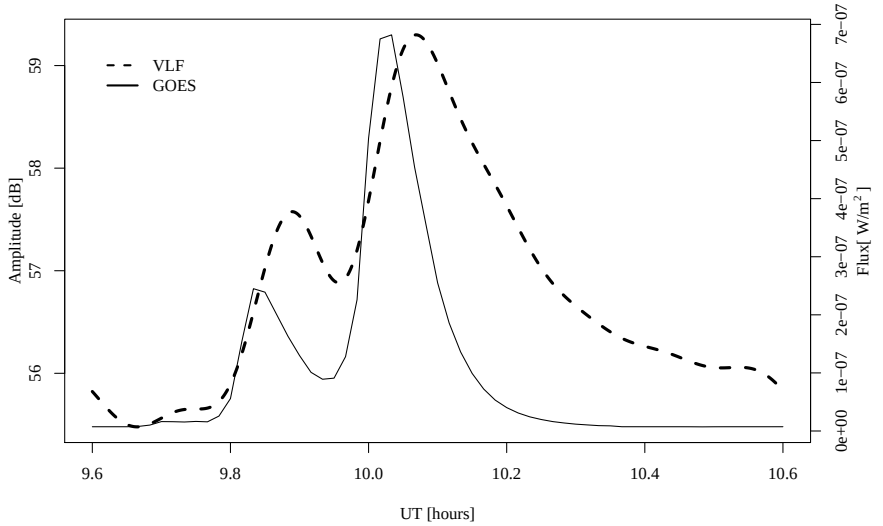

(a) 0.05–0.4 nm, 20.9 kHz Budapest.

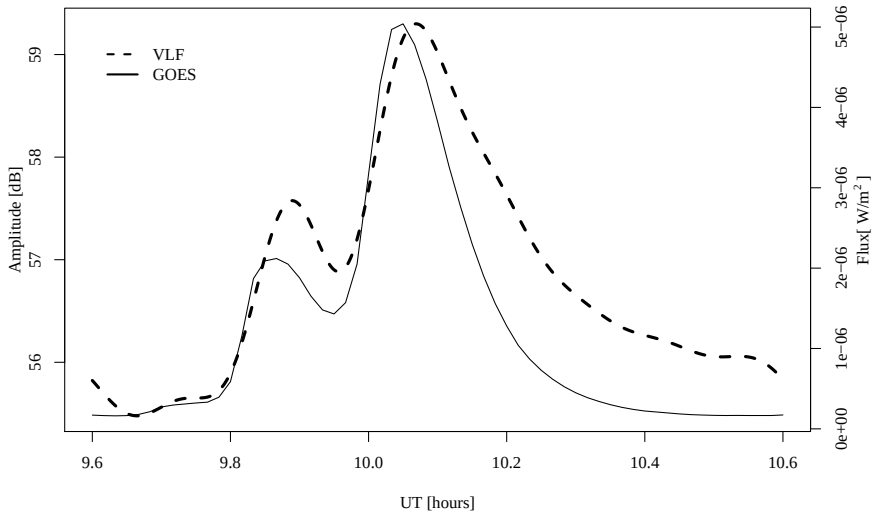

(b) 0.1–0.8 nm, 20.9 kHz Budapest.

Figure 5.30: Amplitude on 13 December 2007 of the 20.9 kHz signal at Budapest with GOES X-ray flux.

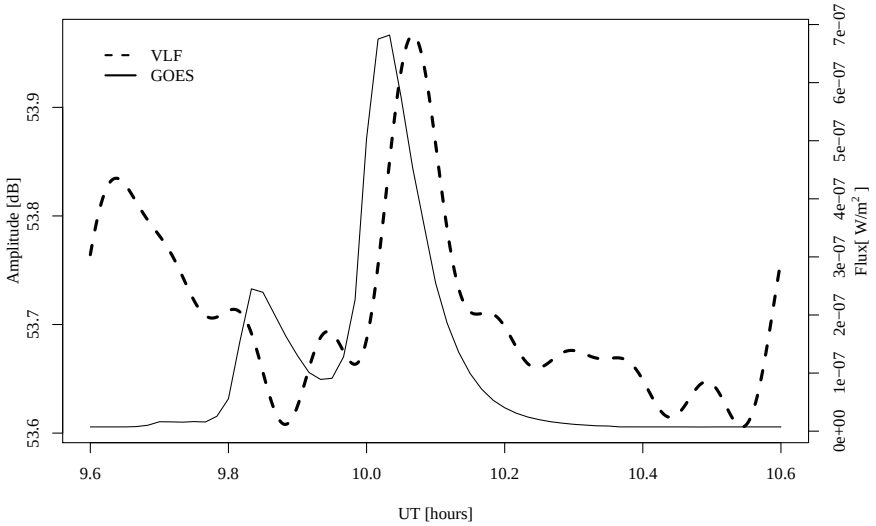

(a) 0.05–0.4 nm, 20.9 kHz Gyergyo.

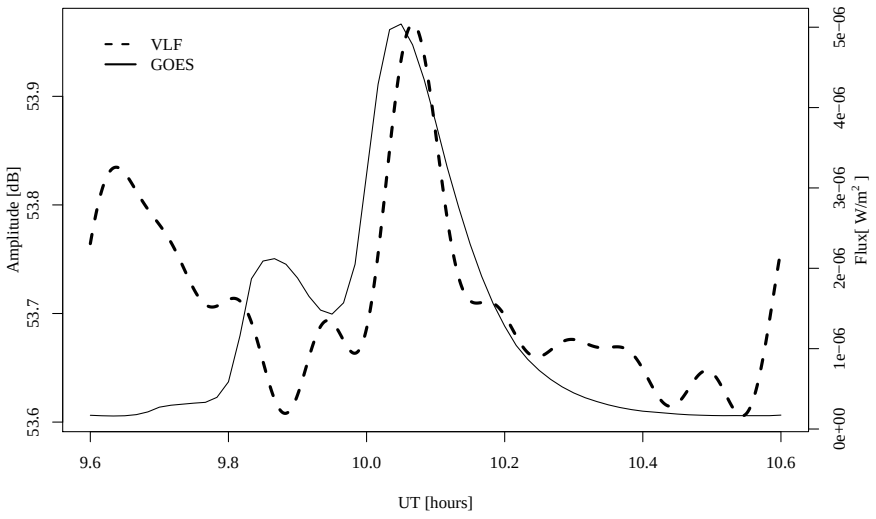

(b) 0.1–0.8 nm, 20.9 kHz Gyergyo.

Figure 5.31: Amplitude on 13 December 2007 of the 20.9 kHz signal at Gyergyo with GOES X-ray flux.

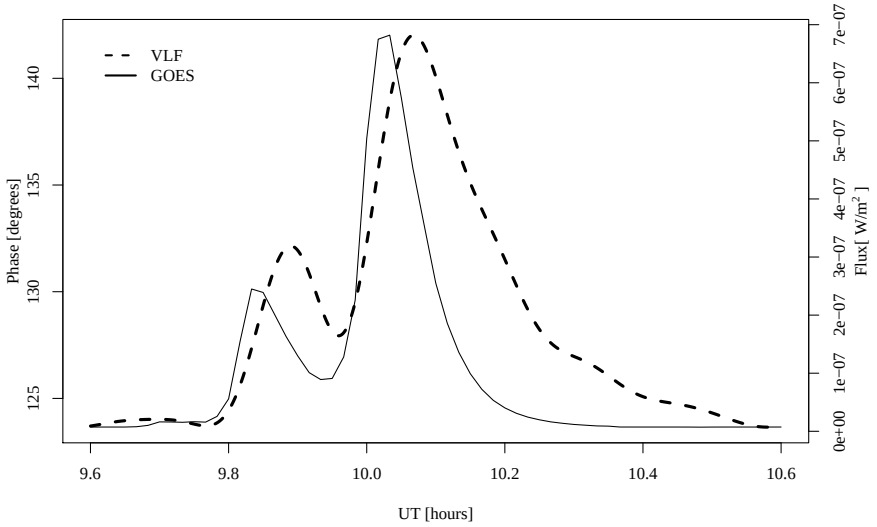

(a) 0.05–0.4 nm, 22.1 kHz Budapest.

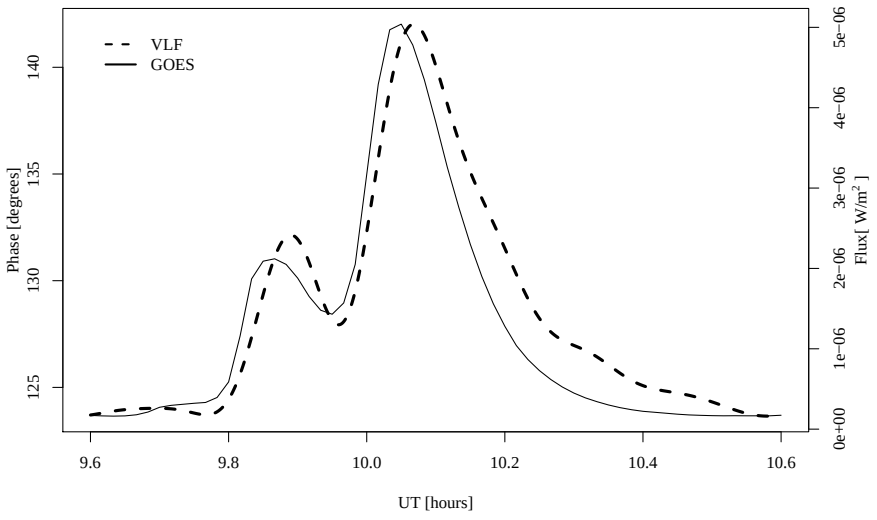

(b) 0.1–0.8 nm, 22.1 kHz Budapest.

Figure 5.32: Phase on 13 December 2007 of the 22.1 kHz signal at Budapest with GOES X-ray flux.

5.5 Case study: 18 December 2007

The 18 December 2007 event is the second largest in magnitude (C2.1) and was recorded on three different propagation paths. The flare was also imaged in several wavelength bands that is provided by Solar Monitor. Solar Monitor monitors an active region and its behaviour until there is no more activity visible and classify it with a number. For example, this region in latitude and longitude from 13 December 2007 still continued to show some activity on 18 December 2007. Figure 5.33 shows the images that were taken of the event. The flare is visible at the limb of the sun in particular the extreme ultraviolet band. It is less apparent in the magnetograms.

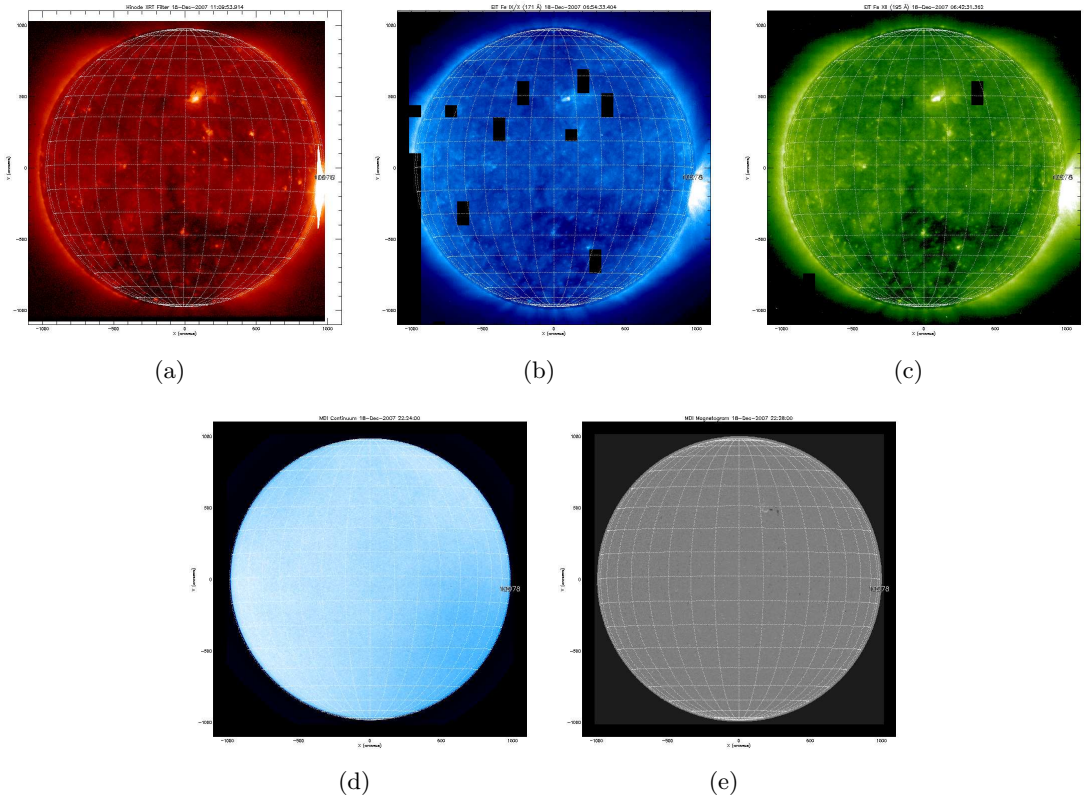

(a) (b) (c)

(d) (e)

Figure 5.33: Images taken of the Sun during the solar flare that occurred on 18 December 2007 (http://www.solarmonitor.org). (a) Hinode/XRT image of the corona in X-ray at 11:09 UT. (b) Extreme Ultraviolet Imaging Telescope, the corona in EUV light, in the 17.1 nm band at 06:54 UT. (c) Extreme Ultraviolet Imaging Telescope, the corona in EUV light, in the 19.5 nm band at 06:42 UT. (d) Michelson Doppler Interferometer (MDI) continuum image, showing the photosphere in white light at 22:24 UT. (e) MDI magnetogram showing the line-of-sight magnetic field in the photosphere at 22:28 UT. The flare is seen at the right edge of the Sun at the top-right part of the bottom-right quadrant. There was no H-α image available for this particular day.

5.5.1 Extracting H' and β

The flare was detected near the end of the day in the VLF data (see Figures 5.18–5.20). The same unperturbed values for H' (75 km) and β (0.32 km^{-1}) were assumed even though the flare occurred at the end of the profile. LWPC is once again used to vary H' and β to match the observations of the amplitude and phase of the signal at the receivers. The average β was 0.34 km^{-1} and 73.7 km for H' at time of maximum change in the amplitude or phase over the propagation paths. The change in β is then given by $\triangle\beta = 0.02$ km^{-1} and for H' it is $\triangle H' = -1.2$ km. A summary is showed in Table 5.4.

Table 5.4: Calculated β and H' values from LWPC for propagation paths for 18 December 2007. $\triangle$A and $\triangle$P are the changes in VLF amplitude and phase.

Frequency (kHz)	Receiver	GCP (distance)	$\triangle$A (dB)	$\triangle$P (deg)	β (km^{-1})	H' (km)
19.6	Tihany	1687	0.38 (inc)	-	0.35	74.0
22.1	Budapest	1540	-	6	0.34	73.7
20.9	Gyergyo	2058	0.72	-	0.34	73..5

5.5.2 Electron density profile and modal interference

Using (1.2) and the values calculated by LWPC the electron density profile is constructed for altitudes z = 60–90 km and is given by Figure 5.34. From Figure 5.34 the increase in the slope from the unperturbed conditions is visible due to the extra ionisation that took place at the time of the flare and therefore increases the electron content at lower altitudes.

The amplitude and phase as a function of the distance from the transmitter are given by Figures 5.35–5.37. The vertical solid lines represent the distance of the receivers from the transmitters. An interference modal minimum for the 19.6 kHz transmitter seems almost unchanged at 680 km and for both the 20.9 kHz and 22.1 kHz transmitters it moved 40 km towards the transmitter, 760 to 720 km and 1000 to 960 km respectively.

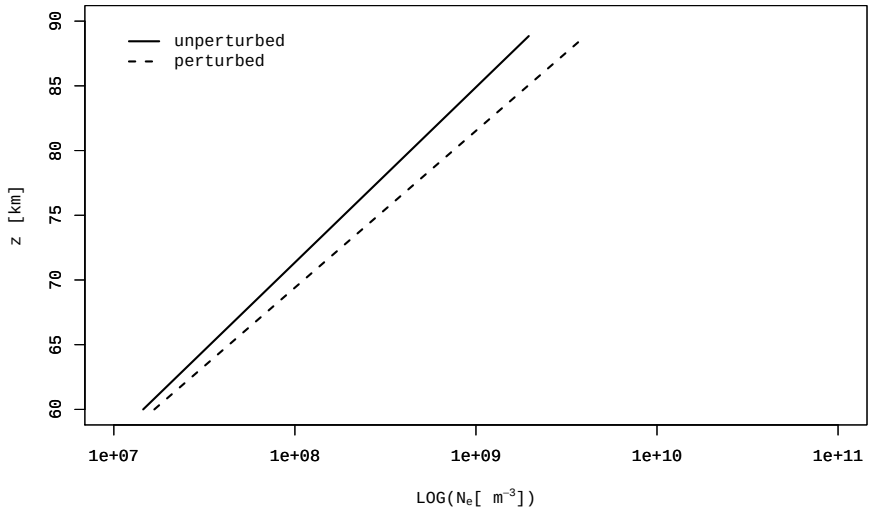

Figure 5.34: Electron density profile on 18 December 2007 for the quiet unperturbed and perturbed ionosphere at the peak of the flare, 13:20 UT.

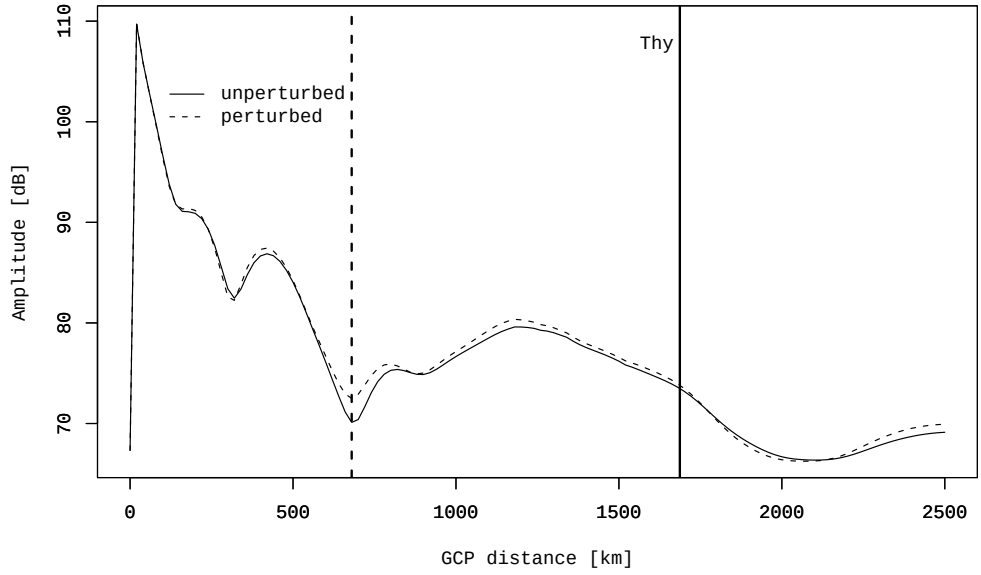

Figure 5.35: Calculated variation in amplitude of the $19.6\ \mathrm{kHz}$ signal as a function of distance along the GCP for 18 December 2007. The vertical dashed line represents an example of a modal minimum for unperturbed conditions.

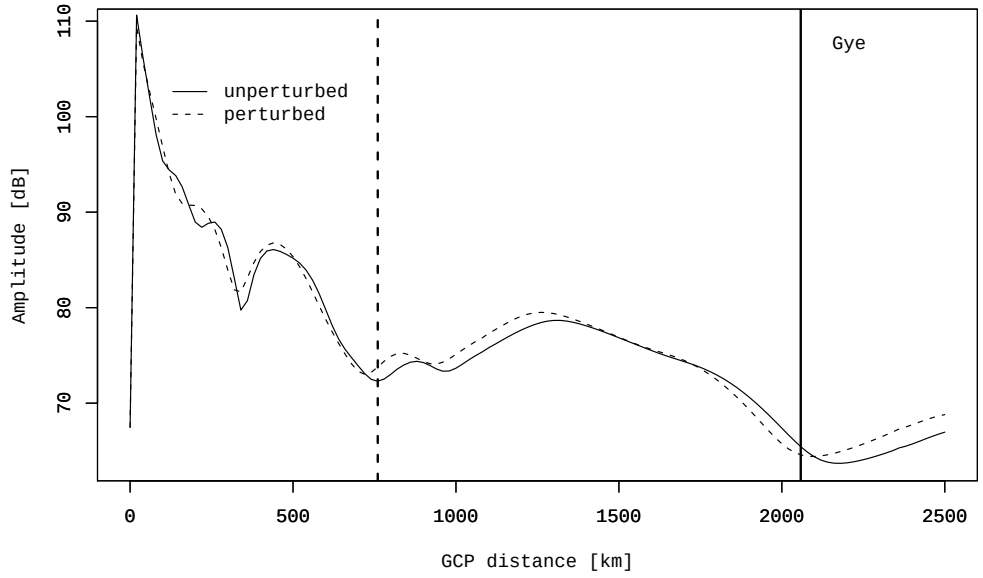

Figure 5.36: Calculated variation in amplitude of the $20.9\ \mathrm{kHz}$ signal as a function of distance along the GCP for 18 December 2007. The vertical dashed line represents an example of a modal minimum for unperturbed conditions.

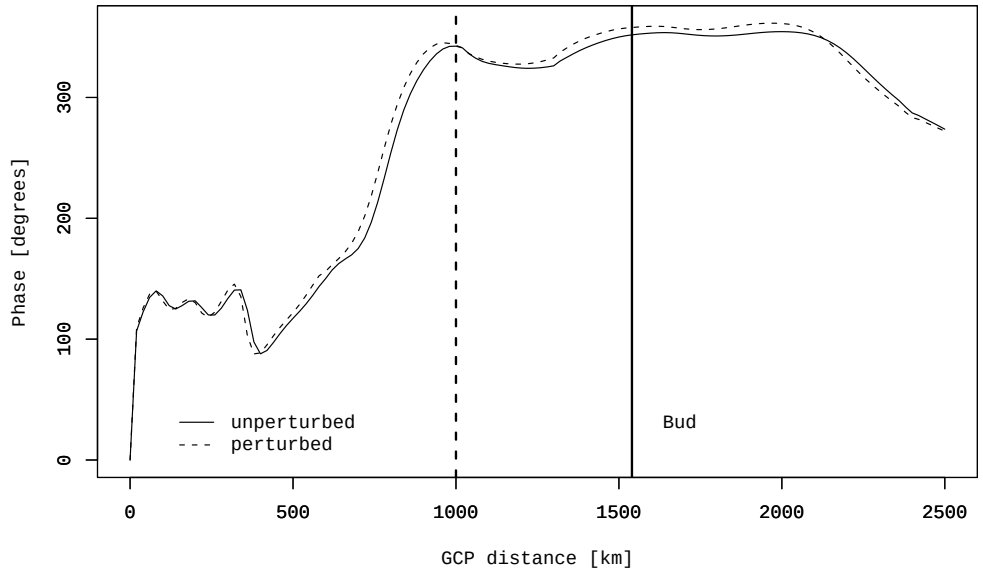

Figure 5.37: Calculated variation in phase of the $22.1\ \mathrm{kHz}$ signal as a function of distance along the GCP for 18 December 2007. The vertical dashed line represents an example of a modal minimum for unperturbed conditions.

5.5.3 Comparing flux data with VLF amplitude and phase data

As discussed earlier with the event of 13 December 2007, a Fourier reconstruction was applied to the VLF data using a low pass filter and removing those components with periods shorter than 0.00249 Hz. The raw data and smoothed curve to the data are shown in Figure 5.38.

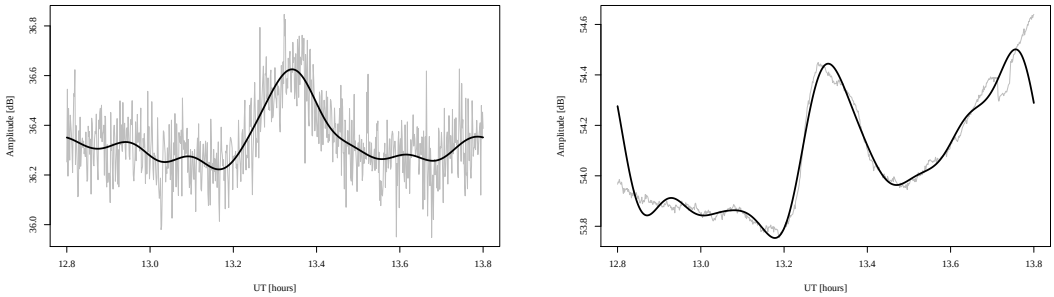

(a) 19.6 kHz, Tihany, amplitude.

(b) 20.9 kHz, Gyergyo, amplitude.

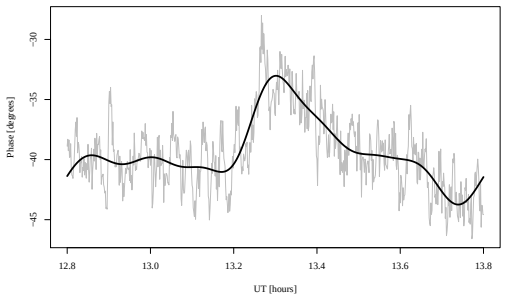

(c) 22.1 kHz, Budapest, amplitude.

Figure 5.38: The fit for 18 December 2007 after a Fourier reconstruction was applied to the VLF data at the different receivers.

In the GOES flux data there is an interval after the flux decreases from the first peak where the flux almost stays constant for a while and then continues decreasing. This, however, is not seen in the VLF data. The profile of the VLF data in most cases seem almost to be too "sharp" compared to the GOES flux profile. The phase data of the 22.1 kHz transmitter appears to be a better fit to the flux profile. Also the 0.1–0.8 nm flux data compares better with the VLF data. The delay between the flux and VLF data is also noticed suggesting that there is a delay in the ionisation of the ionosphere.

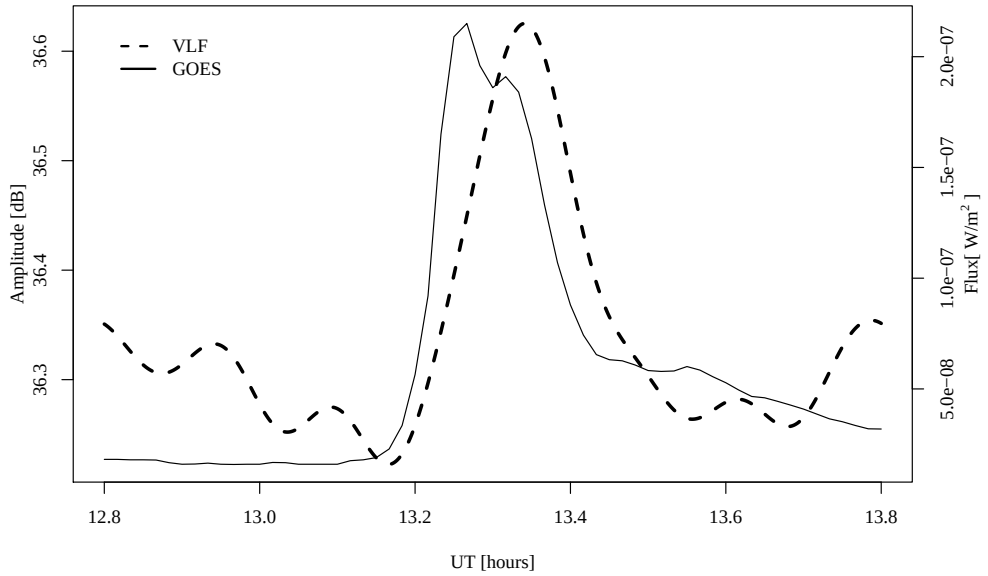

(a) 0.05–0.4 nm, 19.6 kHz Tihany.

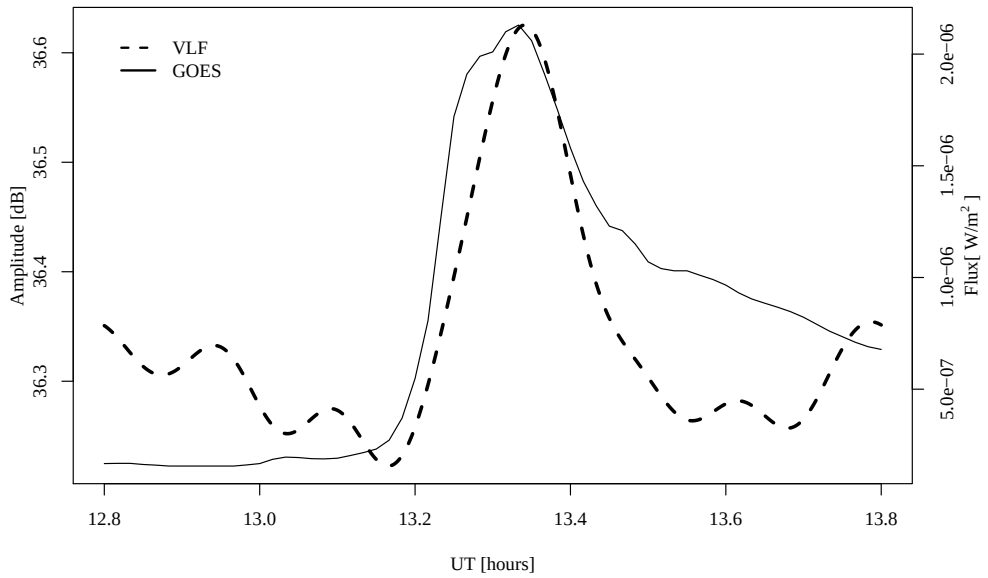

(b) 0.1–0.8 nm, 19.6 kHz Tihany.

Figure 5.39: Amplitude on 18 December 2007 of the 19.6 kHz signal at Tihany with GOES X-ray flux.

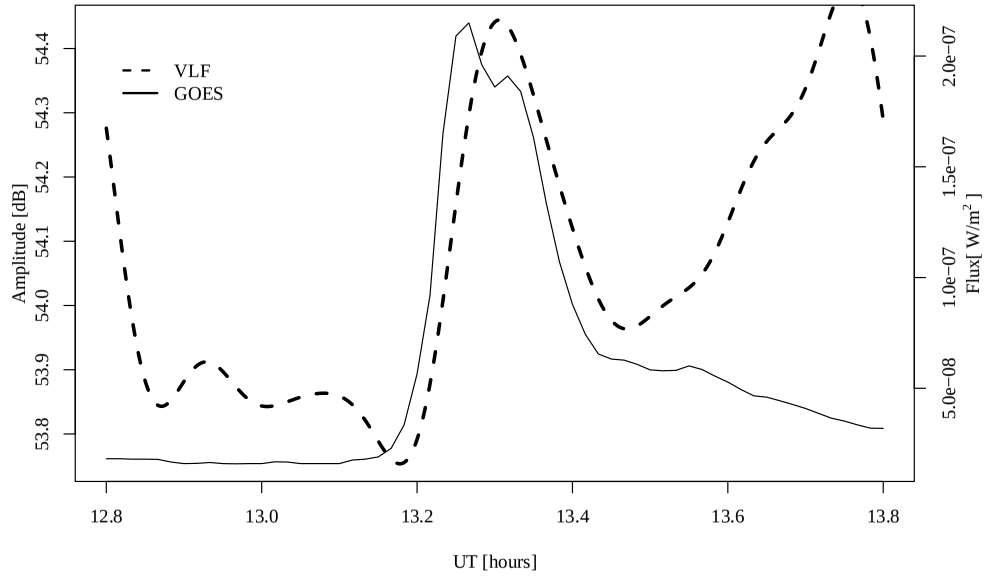

(a) 0.05–0.4 nm, 20.9 kHz Gyergyo.

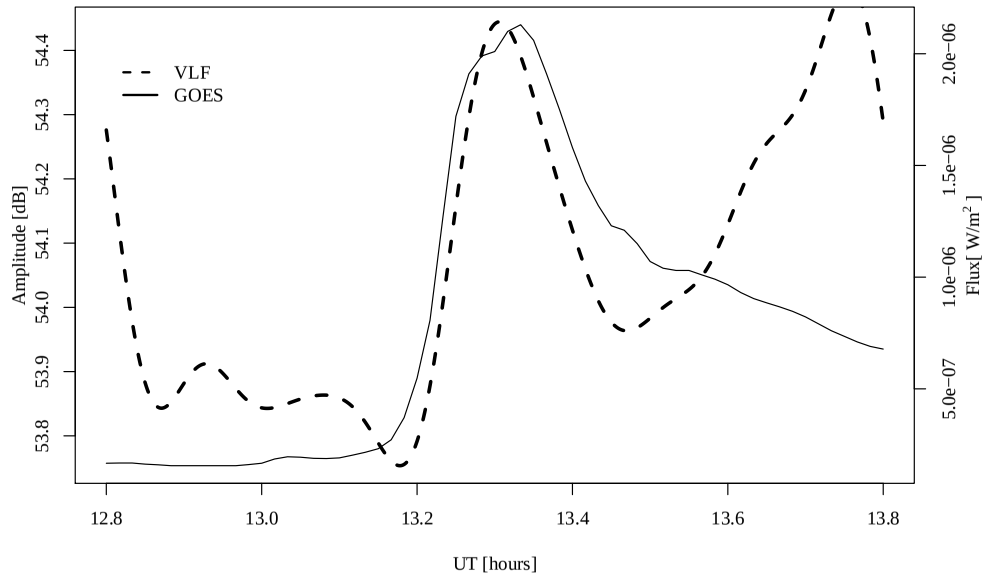

(b) 0.1–0.8 nm, 20.9 kHz Gyergyo.

Figure 5.40: Amplitude on 18 December 2007 of the 20.9 kHz signal at Gyergyo with GOES X-ray flux.

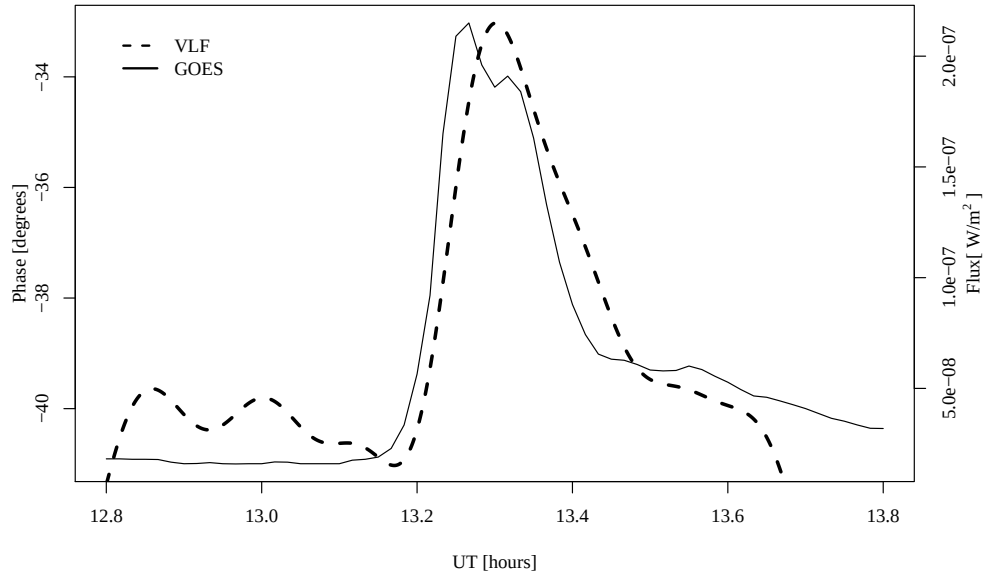

(a) 0.05–0.4 nm, 22.1 kHz Budapest.

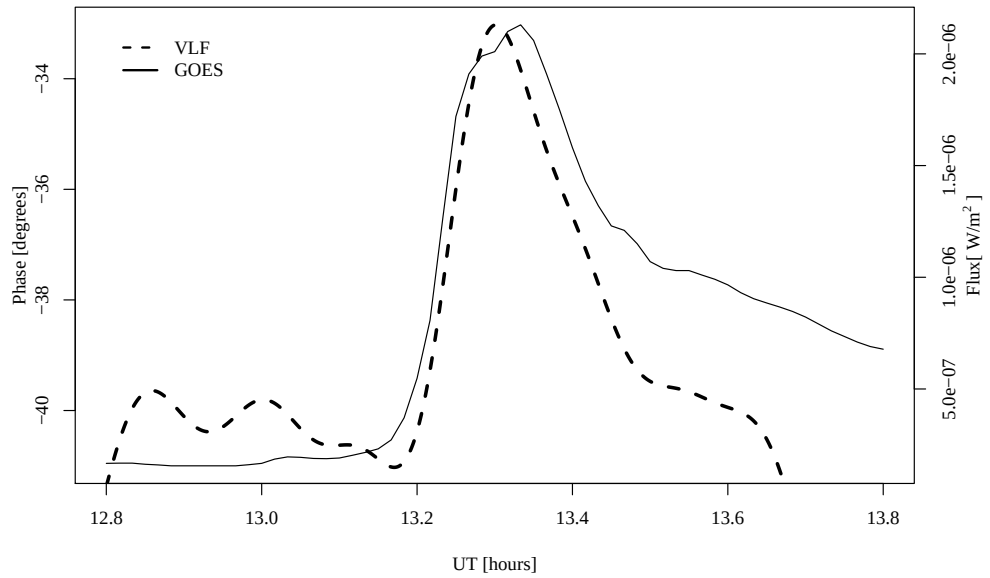

(b) 0.1–0.8 nm, 22.1 kHz Budapest.

Figure 5.41: Phase on 18 December 2007 of the 22.1 kHz signal at Budapest with GOES X-ray flux.

Chapter 6

Discussion

Solar flares are events that occur on the Sun where a large amount of energy is released in the form of electromagnetic radiation. These electromagnetic waves penetrate through the Earth's magnetosphere and ionosphere, enhancing ionisation in the D-region and having an effect on radio communication. Solar flares are usually accompanied by CMEs.

To understand the propagation of specifically VLF waves, a waveguide model was described. The mode theory of VLF propagation was used to describe waves that propagate in a parallel plate waveguide where the upper boundary represents the D-region and the lower boundary the surface of the Earth. From the results of the waveguide theory the different types of modes were derived and discussed, i.e. the TE, TM and TEM modes. It was seen that for each driven frequency there is a cutoff frequency and only modes with frequencies less than the cutoff frequency will contribute to the signal. Specifically the modes of propagation were derived for the day ($H' = 75$ km) and night ($H' = 85$ km) conditions in the ionosphere. As an example, the reflection height was extracted from a broadband VLF spectrum using the mode theory for a specific time during the day at a specific location.

The terminator effects over west-east propagation paths were investigated. From the selected VLF paths some minima were seen in the profile of the VLF data which occurred specifically near sunrise and sunset at the receiver. The number of minima were found to be more for longer propagation paths. The minima were explained as the interference between the original mode and the mode that was excited at the terminator.

The average diurnal amplitude profile was calculated over a period of a month and the months of August 2007 to January 2008 were compared. It was found that the period of depressed amplitude narrows from summer to winter. The change in the maximum and minimum amplitude (day and night) was calculated for each day and averaged for each month and compared to each other. There seemed to be no clear pattern.

In July 2007 until March 2008, a period near solar minimum, 5 flares were identified in the VLF data that was available. There were different propagation paths on which the flares were detected. The events were mainly observed in the amplitude of the signal with the exception of two cases where there was good phase data. An increase or decrease in the amplitude of the signal was observed that depends on the interference between the different modes at the receiver and the attenuation rates of the modes.

Case studies were presented for 13 December 2007 and 18 December 2007 flares with classes of C4.5 and C2.1, respectively. Both events occurred within the same active region of the Sun but on different days. Both events were visible in extreme ultra violet images and magnetograms.

The LWPC code was used to compute the ionospheric parameters. The parameters were varied in the code to modify a waveguide that matched the amplitude and phase observations changes caused by a solar flare.

It was found that the reflection height (H') decreased and the sharpness parameter (β) increased during the time of a flare. The effect was intensified with a greater magnitude flare. For the C2.1 flare, H' decreased by 1.27 km and β increased by 0.023 km^{-1}. For the C4.5 flare, H' decreased by 3.12 km and β increased by 0.070 km^{-1}. The changes in H' and β lead to a change in the electron density profile. At the time of the flare the slope of the electron density profile was found to increase from the unperturbed conditions. The increase in the slope of the electron density profile illustrates how the extra X-rays that were released during the flare ionise the D-region to lower alitudes. The slope of the electron density profile was found to increase with greater magnitude solar flares as β increased for greater solar flares (Figure 6.1). The interference modal minima were found to move towards the transmitter at the time of flare. Once again the effect is intensified by greater flares.

An attempt was made to see how the flare X-ray flux compared with the VLF data. The timescales of the VLF and flux profile were seen to be quite similar. The signature shows up in the VLF data within a few minutes of the flux data. There seems to be a slower recovery in the VLF signal than that observed in the flux data. The phase data was found to compare with the flux data better than the amplitude. Particularly the phase data showed a relationship with the flux data in the 0.1–0.8 nm band rather than for the 0.05–0.4 nm band, which suggests that the 0.1–0.8 nm band is mostly responsible for ionising the D-region. The change in the phase of the VLF signal is seen to be almost linearly proportional to the change in the flux. This differs from Thomson et al. (2004) where they found that the logarithm of the flux nearly linearly scaled the fit of the VLF phase curve. While the flare investigated by Thomson et al. (2004) had a maximum

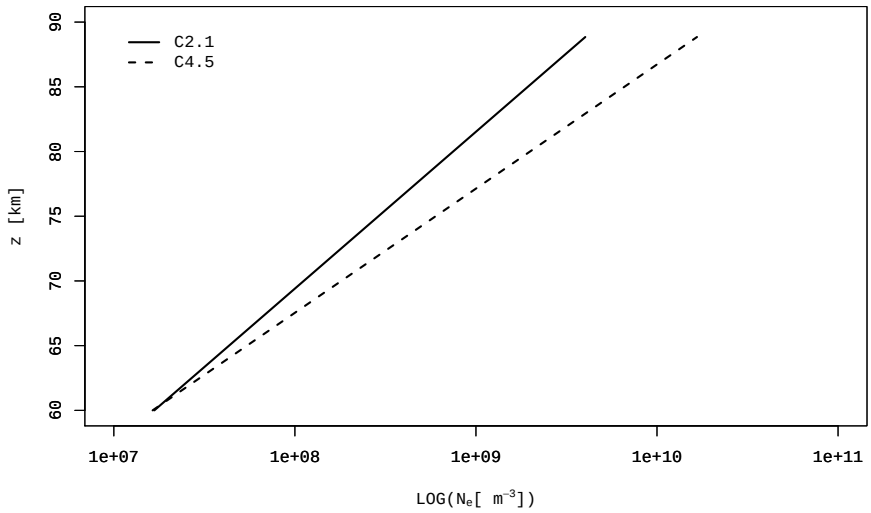

Figure 6.1: Comparison between the electron density profile for the C2.1 and C4.5 flare.

X-ray flux of 1.0 $\mathrm{mW/m^2}$, the greatest flare studied in this thesis only had a flux of 4.5 $\mu\mathrm{W/m^2}$. While the characteristics of the X-ray flux profile for the C4.5 flare, for example the double peak, were more apparent in the VLF data, the VLF profile of the C2.1 flare seemed too narrow compared to the X-ray flux profile in both amplitude and phase.

The results show that solar flares of greater magnitude have a greater effect on the ionospheric parameters, modifying the EIW and therefore having a greater effect on radio communication and observation.

Chapter 7

Conclusion

In the thesis a waveguide model was derived that describes wave propagation in the EIW that is bounded by the Earth's surface and the D-region of the ionosphere. The different modes in which the waves propagate were derived. The characteristics of the modes were used to obtain the reflection height of ionosphere for VLF propagation by using a spectrum of sferics with "tweeks".

An attempt was made to describe VLF observations under quiet and disturbed conditions. The minima occurring in the amplitude versus time profile were explained as interference at the receiver between the original transmitted and the mode created at the terminator. It was found that the terminator caused the depression of the monthly averaged diurnal amplitude profile to narrow from summer to winter.

A series of 5 solar flare events were identified in the VLF data. During of a solar flare it was found that there was a disturbance in the ionospheric parameters. The calculated values for the reflection height, H', were found to decrease and the sharpness parameter, β, to increase during a solar flare. The changes of the ionospheric parameters were intensified with greater magnitude solar flares.

From the calculated values for H' and β an electron density profile was constructed and the gradient of the profile was found to increase as β increased. All the modal interference minima along a propagation path were found to move towards the transmitter during a flare. It was found that in some cases the amplitude and phase were nearly linearly related to the X-ray flux rather than the logarithm of the X-ray flux.

For future purposes, a complete year of data in a time where the Sun is more active would be suggested. Unfortunately there were not that many events of great magnitude. It would prove to be more appropriate to see how H' and β change with a bigger data set of events and where there is a greater variety in the magnitude of the flares. A

further study should be made to see if flares of smaller magnitude relate differently than flares of greater magnitude to X-ray flux data. The only propagation paths that were available here were west-east paths and for completeness north-south propagation paths should also be included.

References

Bain, W. C., Hammond, E., Mar. 1975. Ionospheric solar flare effect observations. Journal of Atmospheric and Solar-Terrestrial Physics 37 (3), 573–574.

Blackband, W. T., 1964. Propagation of Radio Waves at Frequencies Below 300 kc/s. Pergamon Press.

Crombie, D. D., 1964. The effects of a small local change in phase velocity on the propagation of a VLF radio signal. Radio Science 68D, 27.

Crombie, D. D., 1965. On the use of VLF measurements for obtaining information on the lower ionosphere (especially during solar flares). Proceedings of the IEEE 53, 2027–2034.

Davies, K., 1966. Ionospheric Radio Propagation. Peter Peregrinus Ltd.

Eyges, L. (Ed.), 1972. The Classical Electromagnetic Field. Dover Publications.

Ferguson, J. A., 1992. A review of the ionospheric model for the long wave prediction capability TD 2393,Final Report Naval Command, Control and Ocean Surveillance Center.

Ferguson, J. A., Snyder, F. P., Nov. 1980. Approximate VLF/LF waveguide mode conversion model. computer applications: FASTMC and BUMP Progress Report, TD 400, Naval Ocean Systems Center.

Griffiths, D. J. (Ed.), 1999. Introduction to Electrodynamics. Prentice Hall.

Grubor, D. P., Šulić, D. M., Žigman, V., 2008. Classification of X-ray solar flares regarding their effects on the lower ionosphere electron density profile. Annales Geophysicae 26 (7), 1731–1740.

Harrison, R. P., 1974. Demonstration of the transverse electric (TE) mode radio propagation in the Earth-ionosphere waveguide. Air force Cambridge research labs Hanscom AFB MA NTIS Accession No. AD774449.

Kikuchi, T., Jan. 1986. Waveguide model analyses of omega VLF wave propagation at 13.6 kHz. Journal of Atmospheric and Terrestrial Physics 48 (1), 15–23.

Kumar, S., Kumar, A., 2007. Diurnal variation of the 19.8 kHz signal propagation over long path to suva. South Pacific Journal of Natural Science 11, 68.

Lorrain, P., Corson, D. R., Lorrain, F., 1988. Electromagnetic Fields and Waves. W. H. Freeman and Company.

McRae, W. M., Thomson, N. R., 2004. Solar flare induced ionospheric D-region enhancements from VLF phase and amplitude observations. Journal of Atmospheric and Solar-Terrestrial Physics 66, 77–87.

Morfitt, D., Sep. 1977. Effective electron density distributions describing VLF/ELF propagation data. National Technical Information Service Springfield NTIS Accession No. ADA047508 (Naval Ocean Systems Center Technical Report NOSC/TR 141).

R., M. R., 1968. World wide VLF effective conductivity map Westinghouse electric corporation report 8013F-1.

Thomson, N. R., 1993. Experimental daytime VLF ionosphere parameters. Journal of Atmospheric and Solar-Terrestrial Physics 55, 173–184.

Thomson, N. R., Clilverd, A., 2001. Solar flare induced ionospheric D-region enhancements from VLF amplitude observations. Journal of Atmospheric and Solar-Terrestrial Physics 63, 1729–1737.

Thomson, N. R., Rodger, C. J., Dowden, R. L., 2004. Ionosphere gives size of greatest solar flare. Geophysical Research Letters 31, L06803.

Wait, J. R., 1962. Electromagnetic Waves in Stratified Media. Vol. 3 of International Series of Monographs on Electromagnetic Waves. Pergamon Press.

Wait, J. R., Spies, K. P., 1964. Characteristics of the Earth-ionosphere waveguide for vlf radio waves. NBS technical note, 300.

Westerlund, S., Reder, F. H., 1970. VLF radio signal phase instabilities produced by propagation medium. Journal of Atmospheric and Terrestrial Physics 33, 103.

Zinn, J., Sutherland, C., Stone, S., Duncan, L., Behnke, R., 1982. Ionospheric effects of rocket exhaust products - heao-c and skylab. Journal of Atmospheric and Terrestrial Physics 44, 1143–1171.

Zinn, J., Sutherland, C. D., Ganguly, S., 1990. The solar flare of August 18, 1979: Incoherent scatter radar data and photochemical model comparisons. Journal of Geophysical Research 95 (D10), 16705–16718.

Appendix A

The input file of LWPC is called lwpm.inp. The output of the data is stored in the folder `Output\`with the prefix of the files given by `tx.`So in this case the files that will be created from the input are called betahprofile.mds, betahprofile.lwf and betahprofile.grd. LWPC has data for transmitters with their transmitting frequencies, power and location. In the example the transmitter that is used is GBZ in the `tx-data`field. The ionosphere model that is used is given by `ionosphere`and in this case a homogeneous exponential model is used with $\beta = 0.35\ \mathrm{km}^{-1}$ and $H' = 74\ \mathrm{km}$. The receivers are placed with their latitude followed by their longitude next to `receivers`field. A program called lwpm.exe takes the parameters from lwpm.inp and computes the amplitude and phase along a propagation path. Here is an example of the lwpm.inp file that was used to calculate H' and β.

```
file-mds    Output\
file-lwf    Output\
file-grd    Output\
file-prf    Profile\
file-ndx    Profile\
case-id     GBZ transmitting to Budapest
  Name the files
tx          betahprofile
  Identify the transmitter
tx-data     GBZ
  Choose the LWPM model daytime environment
ionosphere homogeneous exponential 0.35 74
receivers 47.47194 -19.05028 46.71667 -25.61667
+receivers 46.9089 -17.87923
start

quit
```